Bacterial cell surface nanoenvironment requires a specialized chaperone to activate a peptidoglycan biosynthetic enzyme

Thomas Delerue[1]*, Sylvia Chareyre[1]*, Vivek Anantharaman[2], Michael C. Gilmore[3], David L. Popham[4], Felipe Cava[3], L. Aravind[2], and Kumaran S. Ramamurthi[1,a]

[1]Laboratory of Molecular Biology, National Cancer Institute, National Institutes of Health, Bethesda, Maryland, USA

[2]National Center for Biotechnology Information, National Library of Medicine, National Institutes of Health, Bethesda, Maryland, USA

[3]The Laboratory for Molecular Infection Medicine Sweden (MIMS), Umeå Center for Microbial Research (UCMR), Science for Life Laboratory (SciLifeLab), Department of Molecular Biology, Umeå University, Umeå, Sweden

[4]Department of Biological Sciences, Virginia Tech, Blacksburg, Virginia, USA

*These authors contributed equally

[a]To whom correspondence should be addressed: ramamurthiks@mail.nih.gov

Keywords: SpoIVA; SpoVM, DivIVA; MreB, FtsZ, Clostridium

ABSTRACT

Bacillus subtilis **spores are produced inside the cytosol of a mother cell. Spore surface assembly requires the SpoVK protein in the mother cell, but its function is unknown. Here, we report that SpoVK is a dedicated chaperone from a distinct higher-order clade of AAA+ ATPases that activates the peptidoglycan glycosyltransferase MurG during sporulation, even though MurG does not normally require activation by a chaperone during vegetative growth. MurG redeploys to the spore surface during sporulation, where we show that the local pH is reduced and propose that this change in cytosolic nanoenvironment necessitates a specific chaperone for proper MurG function. Further, we show that SpoVK participates in a developmental checkpoint in which improper spore surface assembly inactivates SpoVK, which leads to sporulation arrest. The AAA+ ATPase clade containing SpoVK includes other dedicated chaperones involved in secretion, cell-envelope biosynthesis, and carbohydrate metabolism, suggesting that such fine-tuning might be a widespread feature of different subcellular nanoenvironments.**

INTRODUCTION

The use of cytosolic molecular chaperones in aiding proteins that fold improperly in response to harsh environmental conditions has been extensively studied in the context of bacterial stress responses (2-4). Insults such as oxidative stress and extreme temperature and pH can cause protein denaturation and, ultimately, loss of function. As a defense, bacteria have evolved specialized proteins, termed chaperones, that aid protein folding, preventing the aggregation of misfolded proteins, and even resolving protein aggregates. An important group of these chaperones belongs to the AAA+ family, which includes those that assist protein folding in mitochondria, the endoplasmic reticulum, and bacterial cells (5-7).

Spore formation is a developmental program that certain Gram-positive bacteria initiate when faced with starvation (8-10). In *Bacillus subtilis*, sporulation initiates with an asymmetric division event that divides the progenitor cell into two unequally sized daughter cells that will display different cell fates: a smaller forespore that will mature into a dormant cell type called the "spore" and a larger mother cell that will eventually lyse (Fig. 1A). Next, the mother cell engulfs the forespore and builds two concentric shells around the forespore that will eventually protect the mature spore from the environment: an inner peptidoglycan "cortex" built between the double membrane envelope surrounding the forespore, and an outer proteinaceous "coat" built around the outer forespore membrane. The coat is a complex structure consisting of ~80 mother cell-produced proteins (11) whose basement layer is built using SpoIVA, a cytoskeletal protein (12-14) that hydrolyzes ATP to irreversibly assemble around the developing forespore (15-17). Eventually, the mother cell lyses in a programmed manner and releases the mature, dormant spore.

Although the final structure of the cortex peptidoglycan is different from vegetative peptidoglycan, it is built using the same precursors (18). During vegetative growth, the final precursor, the membrane-bound lipid II, is synthesized in the cytosol and flipped to the oxidizing environment of the cell surface; during sporulation, lipid II is synthesized in the mother cell and

flipped into the forespore intermembrane space. Vegetative growth requires peptidoglycan insertion in two different locations: at the lateral edge of the growing cell and at mid-cell during cell division (19-21). Accordingly, specific transpeptidases and transglycosylases are tasked with attaching new cell wall material into the appropriate location and must coordinate their activity with cell membrane formation or the cell division machinery. Although a link between coat assembly and the transglycosylases and transpeptidases that mediate cortex assembly has not been formally established, cortex assembly is nonetheless subject to the coat assembly checkpoint. In this checkpoint, cortex assembly will not initiate unless the basement layer of the coat, composed of SpoIVA, properly polymerizes (22-24). Recently, we reported that the SpoIVA-associated protein SpoVID (25-27) physically monitors the polymerization state of SpoIVA via the C-terminus of SpoVID, which curiously harbors a peptidoglycan-binding domain called LysM (28). When SpoIVA polymerizes properly, the C-terminus of SpoVID binds to the polymerized SpoIVA, occluding the LysM domain. However, if SpoIVA mis-assembles, the C-terminus of SpoVID is liberated, thereby exposing the LysM domain which binds to and sequesters the lipid II precursor in the mother cell cytosol, thereby blocking cortex assembly. Although SpoVID molecules (and therefore LysM domains) vastly outnumber the estimated number of lipid II molecules at any given time (28), it was not clear how the checkpoint could remain functional in the face of additional lipid II synthesis that may overwhelm the lipid II sequestration capacity of SpoVID.

In this study, we employed a genetic strategy to identify additional factors that participate in the coat assembly checkpoint, which yielded the previously uncharacterized AAA+ chaperone SpoVK (29). We report that SpoVK activates the lipid II synthase MurG. During sporulation, MurG redeploys from the mother cell plasma membrane to the forespore surface (30) to generate lipid II for cortex assembly, but MurG does not normally require an activating chaperone during vegetative growth. Examining the pH of the mother cell cytosol immediately adjacent to the forespore surface revealed a cytosolic nanoenvironment where the pH was

lower than the rest of the mother cell cytosol. We propose that MurG is largely nonfunctional in this nanoenvironment and requires activation by SpoVK to function during sporulation. Thus, the contiguous cytosol of the mother cell during sporulation is not uniform and the presence of certain cytosolic nanoenvironments may necessitate assisted protein folding for select proteins. Further, we show that this requirement for SpoVK at the forespore surface offers an additional level of regulation wherein the coat assembly checkpoint can inactivate SpoVK upon sensing coat assembly mistakes to prevent the accumulation of lipid II.

RESULTS

Suppressor mutation in spoVK restores cortex assembly caused by defective SpoIVA variants

SpoIVA hydrolyzes ATP to polymerize irreversibly on the forespore surface to form a stable platform upon which the spore coat assembles (14, 16). Since successful initiation of coat assembly is required to trigger cortex assembly, strains of *B. subtilis* harboring defective SpoIVA variants that do not polymerize properly not only fail to assemble the spore coat, but also do not construct a cortex and are therefore unable to sporulate (31). Previously, we exploited this phenotype to isolate a spontaneous suppressor that would correct the sporulation defect of SpoIVA^{T*}, a defective variant with a disrupted "sensor threonine" that binds, but does not hydrolyze, ATP (17). This genetic selection yielded a loss-of-function mutation in the *spoVID* gene (25). We previously presented evidence that SpoVID participates in a checkpoint that monitors coat assembly and, upon sensing a coat assembly defect, would arrest cortex assembly by sequestering the peptidoglycan intermediate lipid II via a C-terminal LysM domain that is unmasked only when the coat mis-assembles (28). To identify additional factors involved in the communication between coat assembly and cortex formation, we used a similar genetic strategy to isolate additional suppressor mutations that would correct the sporulation defect of *spoIVA*^{T*}, but this time we used a strain harboring two copies of *spoVID* to avoid isolating loss-of-function mutations in *spoVID*. To isolate suppressors, we grew cells in sporulation media and removed nonsporulating and poorly sporulating cells by exposure to 80 ºC for 20 min. Surviving cells were then enriched by repeated dilution of the heat-killed culture into fresh sporulation media, where survivors could germinate and re-sporulate. Whole genome sequencing revealed an extragenic mutation in the *spoVK* gene wherein a cytidyl to thymidyl transition changed the specificity of codon 5 from alanine to valine.

SpoVK (previously misnamed SpoVJ) is a poorly studied sporulation protein produced in the mother cell under the control of the σ^E promoter; deletion of *spoVK* resulted in a severe sporulation defect, but its function has remained mysterious (29, 32). Later, SpoVK was

127 classified as a member of the AAA+ family of P-loop NTPases (7). Since SpoVK had not been
128 previously implicated in coat assembly, we first examined the subcellular localization of the coat
129 protein SpoIVA in the presence or absence of SpoVK. GFP-SpoIVA localizes to the forespore
130 surface (Fig. 1B). In the absence of SpoVK, GFP-SpoIVA localization was similar to WT,
131 indicating that SpoVK is not involved directly in coat basement layer assembly. Nonetheless,
132 deletion of *spoVK* resulted in a ~10^6-fold defect in sporulation efficiency relative to WT (Fig. 1C,
133 lane 3), even though the basement layer appeared to assemble normally.
134 Next, we examined the allele specificity of suppression by *spoVK*^{A5V}. In the presence of
135 WT SpoIVA, complementation of the *spoVK* deletion *in trans* with a single copy of either *spoVK*
136 *or spoVK*^{A5V} at an ectopic chromosomal locus (*amyE*) restored sporulation efficiency to a level
137 similar to WT (Fig. 1C, lanes 4-5). In the presence of *spoIVA*^{T*} (the *spoIVA* allele used to isolate
138 the *spoVK*^{A5V} suppressor mutation) or alleles of *spoIVA* in which the Walker B or Walker A
139 motifs were disrupted (*spoIVA*^{B*} and *spoIVA*^{A*}), which abrogates ATP hydrolysis or binding,
140 respectively (17, 33), introducing the *spoVK*^{A5V} allele also suppressed the sporulation defect
141 caused by the mutant *spoIVA* allele (Fig. 1C, lanes 6-17), indicating that suppression by the
142 *spoVK*^{A5V} mutation is not allele-specific.
143 SpoIVA variants that are defective in ATP hydrolysis or binding display subtle
144 localization defects in vivo: GFP-SpoIVA^{B*} and GFP-SpoIVA^{T*} fail to fully encircle the forespore
145 and GFP-SpoIVA^{A*} is predominantly cytosolic (Fig. 1D). Introducing SpoVK^{A5V} did not restore
146 proper localization of these SpoIVA variants (Fig. 1D), despite largely correcting the sporulation
147 defect caused by these SpoIVA variants (Fig. 1C). When viewed by light microscopy, mature
148 WT spores appear as “phase bright” (Fig. 1E) due to the exclusion of water from the spore core,
149 which is maintained by a robust cortex that may be observed using transmission electron
150 microscopy (Fig. 1I, 1M; indicated in yellow). In contrast, cells harboring a defective *spoIVA*
151 allele, such as *spoIVA*^{B*}, that mis-assemble the coat produce “phase gray” spores (Fig. 1F) and
152 fail to build a cortex (Fig. 1J, N). The presence of SpoVK^{A5V} did not affect the morphology of

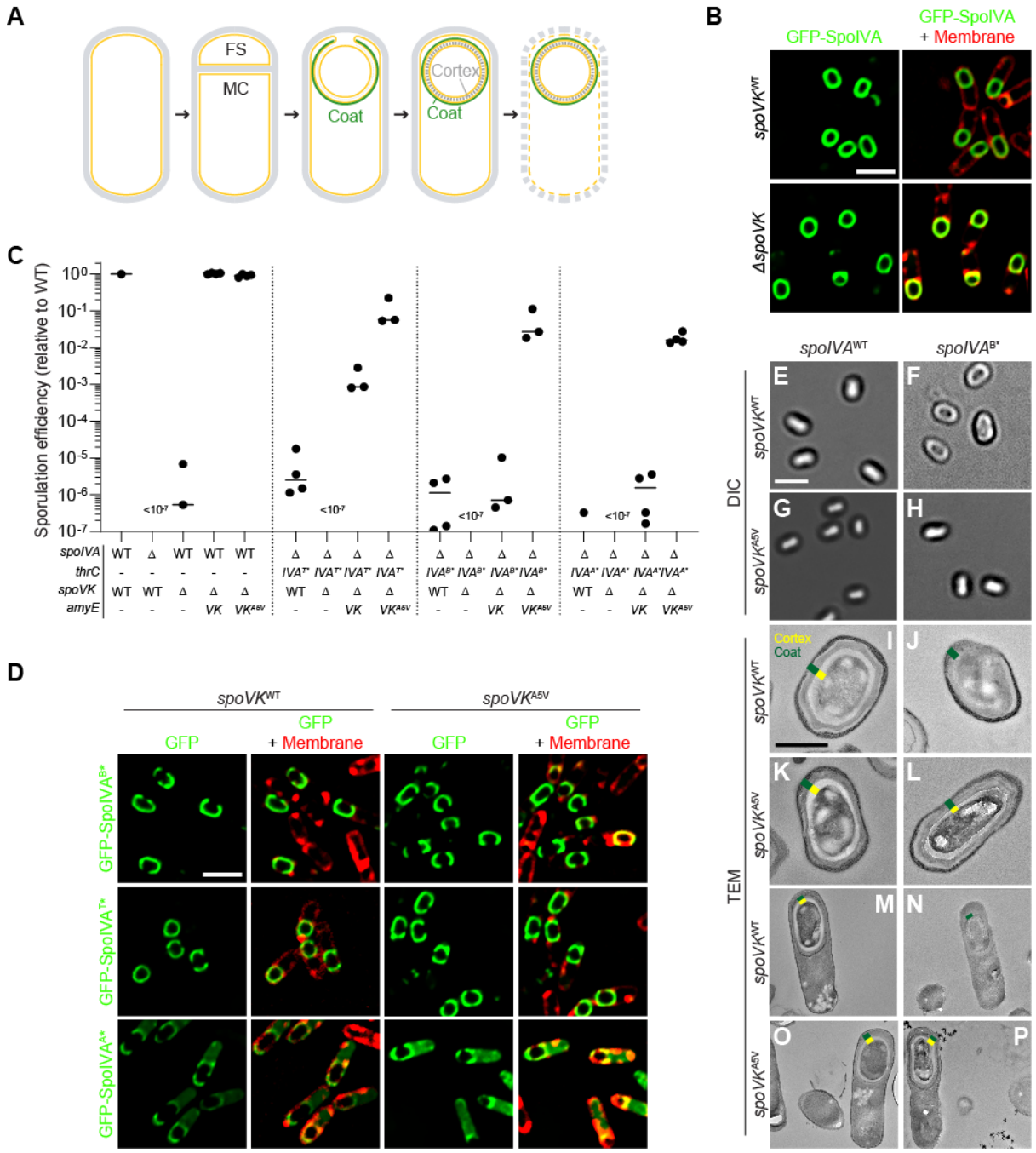

Figure 1. Point mutant in *spoVK* suppresses spore envelope assembly defects caused by mis-assembly of the spore coat basement layer. (A) Schematic representation of sporulation in *Bacillus subtilis*. Asymmetric division results in the formation of a small forespore (FS) and larger mother cell (MC). A proteinaceous shell, the "coat" (green) is first constructed on the outer forespore membrane; a peptidoglycan shell, the "cortex" (gray dashes) is later constructed between the two membranes surrounding the forespore. The mother cell ultimately lyses, releasing the mature forespore into the environment. Membranes are depicted in yellow; peptidoglycan cell wall is depicted in gray. (B) Subcellular localization of GFP-SpoIVA (green) in presence (top panels) or absence (bottom panels) of *spoVK*, 3.5 h after induction of sporulation (strains: KR160 and TD549). Membranes visualized using fluorescent dye FM4-64 (red; right panels). (C) Sporulation efficiencies, determined as resistance to heat, relative to WT (strain PY79). Strain genotypes at *spoIVA* and *spoVK* loci are indicated below the graph; *thrC* and *amyE* are ectopic chromosomal loci used to complement *spoIVA* and *spoVK* deletions, respectively, with different alleles of those genes. Bars represent mean values. Strains: PY79, KP73, TD520, TD513, TD514, JPC221, TD524,

TD530, TD531, TD523, TD528, TD529, KR438, TD817, TD818, and TD819. (D) Subcellular localization of GFP-SpoIVA^{B*}, GFP-SpoIVA^{T*}, or GFP-SpoIVA^{A*} variants that fails to polymerize, in cells producing SpoVK^{WT} (left) or SpoVK^{A5V} (right; strains: TD845, TD846, TD854, TD848, TD849, and TD855) 4 h after induction of sporulation. Left: fluorescence from GFP; right: overlay, fluorescence from GFP and membranes visualized with FM4-64. Size bars: 2 μm. (E-L) Released spores visualized using (E-H) differential interference contrast (DIC) light microscopy (size bar: 2 μm), or (I-L) transmission electron microscopy (TEM; size bar: 500 nm) harboring WT (left) or B* alleles (right) of *spoIVA* in the presence of *spoVK^{WT}* (E-F; I-J) or *spoVK^{A5V}* (G-H; K-L). (M-P) TEM images of strains in (I-L) at 5.5 h after induction of sporulation. Coat (green) and cortex (yellow) are marked, when present, in (I-P). Strains: PY79, JB103, TD514, and TD529. Strain genotypes are listed in Table S2.

otherwise WT cells (Fig. 1G, 1K, 1O), but did restore phase brightness and cortex assembly to cells that harbored *spoIVA^{B*}* (Fig. 1H, 1L, 1P). The results are consistent with a model in which SpoVK participates in the pathway linking coat and cortex assembly, and that *spoVK^{A5V}* is a gain-of-function allele that permits the cell to build a functional cortex even if the basement layer of the spore coat is defective.

SpoVK is an ephemeral forespore-associated protein involved with cortex assembly

In the absence of SpoVK, cells produced phase gray spores which, when viewed by TEM, did not harbor a cortex (Fig. 2A, top row). At 5.5 h after sporulation initiation, WT cells, viewed by TEM, produced a thick cortex, but cells lacking SpoVK instead displayed a thin layer of peptidoglycan surrounding the forespore (Fig. 2A, bottom row, arrow) that excluded the negative stain. To test if this thin peptidoglycan layer was chemically different from cortex peptidoglycan, we extracted cortex peptidoglycan from sporulating WT and Δ*spoVK* cells, digested with mutanolysin, identified and quantified the muropeptides by their characteristic elution times when separated by HPLC, and calculated peptidoglycan structural parameters (34). The levels of three muropeptides that are characteristic of cortex peptidoglycan (muramic acid present as lactam, disaccharide units in tetrasaccharide, and disaccharide units in hexasaccharide) were reduced in the Δ*spoVK* cells compared to WT (Fig. 2B, Table S1). In contrast, levels of three characteristics that are underrepresented in cortex peptidoglycan but are present in vegetative peptidoglycan and in the innermost “germ cell wall” layer of the cortex (muramic acid with tetrapeptide, disaccharide units in disaccharide, and peptide present as

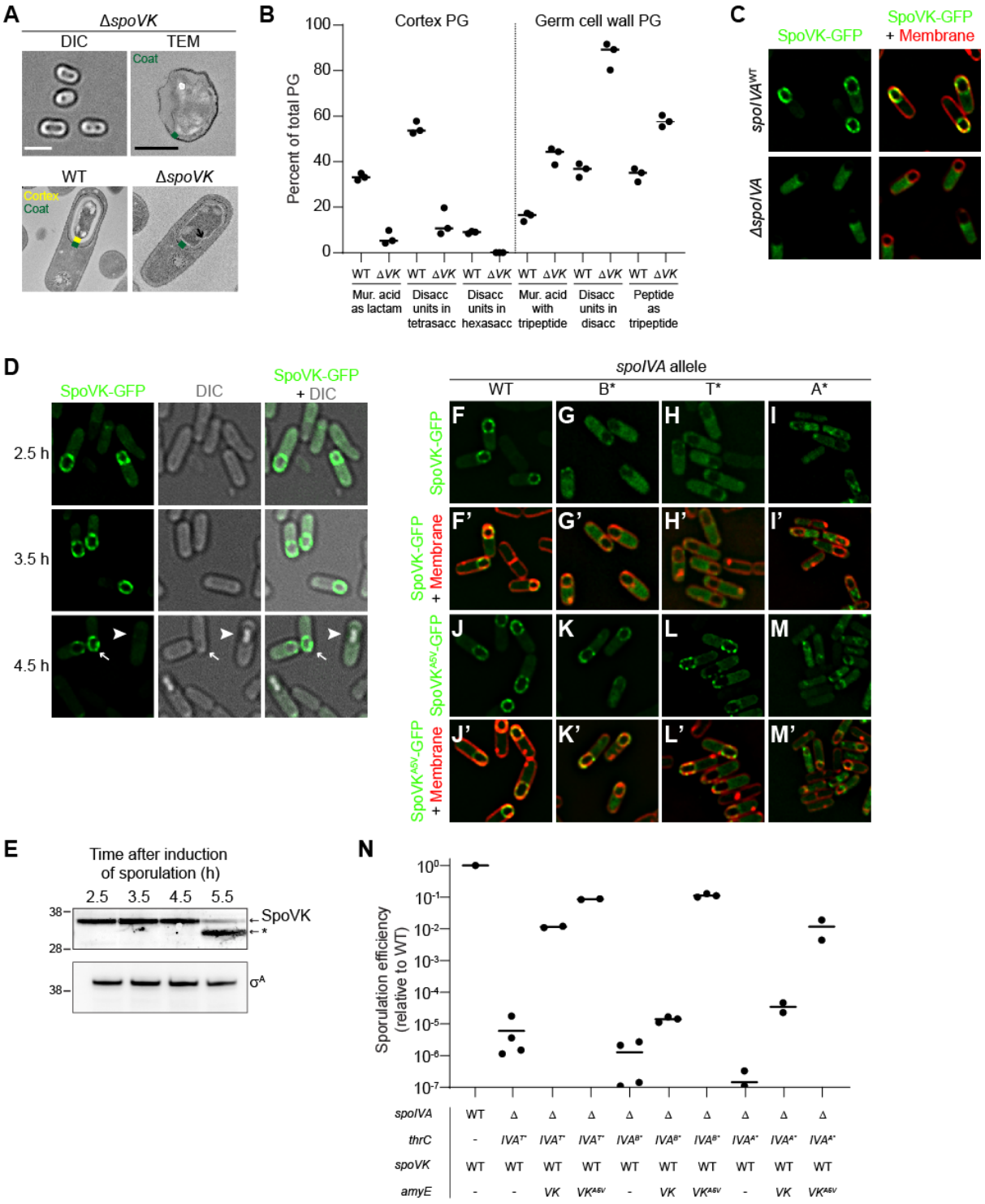

Figure 2. SpoVK is an ephemeral sporulation protein. (A) DIC light microscopy (left; size bar: 2 μm) or TEM images (F; size bar: 500 nm) of released spores (top panels) containing deletion of *spoVK* (strain TD520). Bottom panels: TEM images of WT (left) or *spoVK* deletion strain at 5.5 h after induction of sporulation. Green in the TEM images indicates coat; yellow indicates cortex. (B) Structural parameters of spore peptidoglycan produced by WT or Δ*spoVK* (strains PY79 and TD520, respectively). Peptidoglycan from developing spores was extracted 5 h after induction of sporulation, digested with mutanolysin, and separated by HPLC. Peaks of select muropeptides that are characteristic cortex or germ cell wall were integrated and depicted as a percent of total peptidoglycan (see

Table S1 for complete analysis). Bars represent mean; data points represent an independent culture. (C) Subcellular localization of SpoVK-GFP in presence (top panels) or absence (bottom panels) of *spoIVA* 3.5 h after induction of sporulation (strains TD604 and TD652). Left: fluorescence from SpoVK-GFP; right: overlay of GFP fluorescence (green) and FM4-64 (red). (D) Subcellular localization of SpoVK-GFP at the indicated (left) time points after the induction of sporulation. Left panels: fluorescence from SpoVK-GFP; center: DIC; right: overlay of fluorescence and DIC. Arrowhead indicates a phase bright forespore; arrow indicates phase gray forespore (strain TD604). (E) Immunoblot of cell extracts of sporulating wild type *B. subtilis* (strain PY79) using anti-SpoVK or anti-σ^A antisera, from cells harvested 2.5 h, 3.5 h, 4.5 h, and 5.5 h. Relative mobility of molecular weight markers (kDa) indicated to the let; asterisk indicates a likely degradation product of SpoVK. (F-M') Subcellular localization of (F-I') SpoVK-GFP or (J-M') SpoVK^{A5V}-GFP in the presence of (F-F'; J-J') SpoIVA^{WT} or (G-M') SpoIVA variants that fails to polymerize (IVA^{B*}, IVA^{T*} or -IVA^{A*}) 3.5 h after the induction of sporulation (strains: TD675, TD682, TD684, and TD836). (F-M) GFP fluorescence; (F'-M') overlay, GFP fluorescence and FM4-64. (N) Sporulation efficiencies, determined as resistance to heat, relative to WT (PY79). Strain genotypes at *spoIVA* and *spoVK* loci are indicated below the graph; *thrC* and *amyE* are ectopic chromosomal loci used to complement *spoIVA* and *spoVK* deletions, respectively, with different alleles of those genes. Bars represent mean values; data points represent an independent culture (Strains PY79, JPC221, TD563, TD564, JPC75, TD557, TD558, KR438, TD859, and TD860).

tripeptide) were higher in the Δ*spoVK* cells compared to WT (Fig. 2B). The results suggest that SpoVK is required for producing the structurally distinct cortex peptidoglycan during sporulation.

We next examined the subcellular localization of SpoVK-GFP. In otherwise WT cells, SpoVK-GFP localized as puncta at the periphery of the forespore (Fig. 2C). In the absence of SpoIVA, SpoVK-GFP was instead localized in the mother cell cytosol (Fig. 2C). This genetic dependence on SpoIVA for forespore localization is characteristic of spore coat proteins (11). To test if, like other coat proteins, SpoVK remains associated with the mature spore, we examined SpoVK-GFP localization in sporulating cells at different time points. At 2.5 h and 3.5 h after induction of sporulation, SpoVK-GFP remained associated with the forespore periphery (Fig. 2D). However, at later time points, specifically in cells that had elaborated a phase-bright forespore, SpoVK-GFP was undetectable (Fig. 2D). To ensure that the disappearance of SpoVK-GFP in these cells was not due to loss of fluorescence of the GFP fusion, we examined the presence of native SpoVK in sporulating cells by immunoblotting. SpoVK was detectable in cell extracts at early time points, but at 5.5 h after induction of sporulation, the level of full length SpoVK was diminished and a faster migrating species, likely a SpoVK degradation product, accumulated (Fig. 2E). Thus, SpoVK temporarily associates with the forespore surface in a SpoIVA-dependent manner and is likely degraded once cells elaborate a mature cortex.

193 To understand the role of the A5V substitution in suppressing defective alleles of
194 *spoIVA*, we examined the subcellular localization of SpoVK^{A5V}-GFP. In the presence of ATP
195 hydrolysis-defective variants of SpoIVA (B* and T*), SpoVK-GFP mis-localized in the mother
196 cell cytosol (Fig. 2F-H, F'-H'), but SpoVK^{A5V}-GFP largely correctly localized to the forespore
197 surface despite a defective coat basement layer (Fig. 2J-L, 2J'-2L'). In the presence of the ATP
198 binding-defective SpoIVA variant (A*), the mis-localization of SpoVK-GFP was more
199 pronounced (Fig. 2I, 2I'), but the A5V substitution nonetheless restored at least partial
200 localization to the forespore periphery (Fig. 2M-M'). We next tested if the A5V substitution
201 resulted in a gain of function in SpoVK by examining sporulation efficiency in merodiploid
202 strains. In the presence of SpoIVA variants harboring defects in the nucleotide-binding pocket,
203 addition of a single copy of WT *spoVK* improved the sporulation efficiency slightly (*spoIVA*^{B*}) or
204 ~10^2-10^3-fold (*spoIVA*^{A*} and *spoIVA*^{T*}); the addition of *spoVK*^{A5V} improved sporulation efficiency
205 even further (~10^4-10^5 fold; Fig. 2N). We therefore conclude that SpoVK is a short-lived spore
206 coat-associated protein and that *spoVK*^{A5V} is a gain-of-function allele.
207
208 *SpoVK is a AAA+ ATPase specific to sporulating Firmicutes*
209 While SpoVK has been recognized as an AAA+ ATPase, its affinities within this vast and
210 functionally diverse family of P-loop NTPase enzymes remain poorly understood. Hence, we
211 conducted a systematic evolutionary and structural investigation of SpoVK using sensitive
212 sequence profile analysis, phylogenetic tree construction, and structural modeling. Profile-profile
213 comparisons revealed that it is a member of the "Classical AAA'' assemblage prototyped by the
214 proteasomal subunits, the chaperone CDC48 and FtsH (HHpred p=97-99.5%). Phylogenetic
215 analysis revealed that within that assemblage, SpoVK belongs to a higher-order clade that
216 specifically unites it with SpoVK-like ATPases, the ribulose bisphosphate carboxylase
217 (RuBisCO) chaperone CbbX and its relatives, the Type VII secretion system (T7SS) EccA-like
218 chaperones, and other poorly characterized eukaryotic proteins predicted to play a role in RNA

processing (Fig. 3A). This higher-order clade is, in turn, a sister group of the FtsH AAA+ domains within the Classical AAA assemblage, which share the unifying structural feature of a bihelical hairpin immediately upstream of the Walker A motif (Fig. S1A-B). The apex of this hairpin binds the adenine moiety of the bound nucleotide. This clade is unified by and distinguished from FtsH by: (i) a conserved tyrosine in the sensor-1 region as part of a GY signature; (ii) a conserved asparagine 4 residues upstream of the first arginine finger; and (iii) the presence of the second arginine finger (sensor-2) that is usually lost in FtsH (Fig. S1B). Within the higher-order clade, SpoVK and related proteins emerged as most closely related to the chaperone CbbX (Fig. 3A, S1C).

The N-terminal region of this clade of AAA+ proteins shows considerable variability and features multiple alternative domains (Fig. 3A; e.g., TPRs and a β-helix in EccA, a β-prism in certain CbbX-like versions, and SF-1 RNA helicase domain in eukaryotic representatives) that are indicative of mediating interactions which might recruit the substrate. Our analysis revealed the SpoVK proteins have a short, unique N-terminal domain with 3 β-strands and an α-helix (Fig. S1B). The A5V substitution lies in this region and is predicted to stabilize the first strand of the N-terminal domain keeping with its gain-of-function phenotype. Our phylogenetic analysis also helped objectively discriminate SpoVK from other members of this clade like CbbX or EccA and thereby allowed us to accurately infer its phyletic patterns (Fig. S2). We used this revised phyletic pattern of SpoVK along with those of other related AAA+ ATPases and sporulation proteins to construct a phyletic correlation matrix and extract a functional interaction network from it. This indicated that SpoVK is only found in sporulating firmicutes and is part of a functional interaction network that includes SpoIVA, SpoVID, CotE, and SafA (Fig. 3B). The phyletic patterns further suggest that SpoVK might function downstream of SpoIVA and in parallel with SpoVID (or another factor that harbors a SPOCS and LysM domain such as SipL) in a sporulation specific network (Fig. 3C, Fig. S2). In contrast to the proteasomal, FtsH and CDC48 AAA+ ATPases with rather generic targets, the characterized members of the higher-

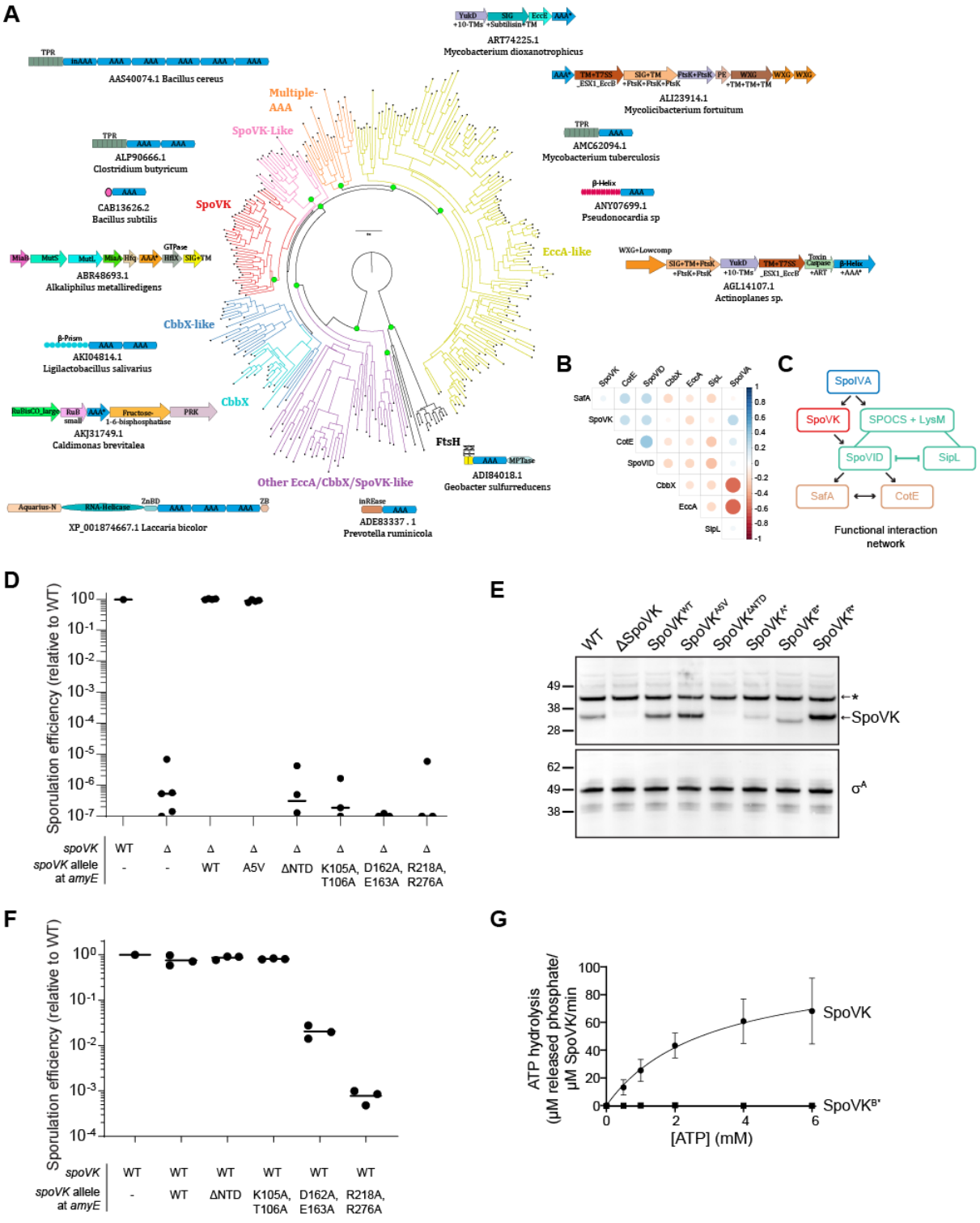

Figure 3. SpoVK is a functional triple AAA+ protein. (A) Phyletic analysis of the SpoVK-EccA-like clade. A phylogenetic tree of a representative set of AAA+ domains in the SpoVK-EccA-like clade is shown. The tree shows the relationship between the SpoVK, SpoVK-like, CbbX, CbbX-like, and EccA-like families and the closest outgroup FtsH. Branches are colored according to the families. Select operonic arrangements or domain architectures of proteins are shown and placed near the branch of the tree in which they or their orthologs occur. Each arrow in the operon is a gene coding for the protein. The accession and organism of the AAA+ containing protein in the operon,

marked with an asterisk, is shown below each operon or domain architecture. ZnBd: zinc-binding. (B) Correlation matrix of SpoIVA, SpoVK, CbbX, EccA, SafA, and SPOCS domain-containing proteins SpoVID, CotE, and SipL/DUF3794 was computed from their phyletic pattern vectors. Color intensity and the size of the circle are proportional to the correlation coefficient. (C) A correlation network of SpoIVA, SpoVK, CbbX, EccA, SafA, and SPOCS domain-containing proteins SpoVID, CotE, and SipL/DUF3794 was computed from this matrix and the phyletic pattern vectors. The nodes and edges are colored as per their functional subgroup in the sporulation system. The arrowheads indicate positive correlations and point from the phyletically more widespread to the less widespread proteins. The flat heads indicate negative correlations. Lines indicate a split in a functionally equivalent family into sub-groups (e.g., SipL and SpoVID).
(D) Sporulation efficiencies, determined as resistance to heat, relative to WT (PY79). Strain genotypes at the *spoVK* locus are indicated below the graph; *amyE* is an ectopic chromosomal locus used to complement the *spoVK* deletion strain with the indicated allele of *spoVK*. Bars represent mean values. Strains: PY79, TD520, TD513, TD514, TD574, TD575, TD576, and TD578. (E) Immunoblot of cell extracts of sporulating *B. subtilis* using anti-SpoVK or anti-σ^A antisera, from cells harvested at 4 h after induction of sporulation. Strains: PY79, TD520, TD513, TD514, TD574, TD575, TD576, and TD578. (F) Sporulation efficiencies, determined as resistance to heat, relative to WT (PY79). Strain genotypes at *spoVK* locus are indicated below the graph; *amyE* is an ectopic chromosomal locus used to produce a merodiploid strain containing two alleles of *spoVK*. Bars represent mean values. Strains: PY79, TD597, TD598, TD599, TD600, and TD602. (G) Saturation curve for ATP hydrolysis by purified SpoVK and SpoVK variant harboring a disrupted Walker B motif (D162A, E163A). Purified SpoVK or SpoVK$^{D162A, E163A}$ was incubated with increasing concentrations of ATP, and nucleotide hydrolysis was assayed by measuring the generation of free phosphate. Data were fit to the Michaelis-Menten enzyme saturation model.

order clade containing SpoVK function as chaperones with “narrow” roles directed at a dedicated target (like RuBisCo in the case of CbbX) or in a specific sub-cellular context (like EccA, which operates on T7SS substrates) (35). Hence, we predict that SpoVK might likewise function as a dedicated chaperone in a specific sporulation-related context.

SpoVK displays ATPase activity *in vitro*

To test if SpoVK is a functional AAA+ NTPase, we first disrupted the conserved Walker A and Walker B motifs and the first arginine finger upstream of strand-5 (Fig. S1A). Disruption of any of these motifs resulted in severe sporulation defects, similar to deletion of the *spoVK* gene (Fig. 3D, lanes 6-8). Examination of cell extracts of sporulating cells by immunoblotting revealed that disruption of the Walker A or Walker B motifs, but not the arginine finger, reduced, but did not eliminate, accumulation of SpoVK protein relative to WT SpoVK (Fig. 3E, lanes 6-8). Next, we examined the role of the N-terminal domain (NTD; residues 2-41), which might recruit substrates as in other AAA+ proteins. Deletion of the NTD completely abrogated accumulation of SpoVK (Fig. 3E, lane 5), and consequently resulted in reduced sporulation efficiency, similar to deletion of the *spoVK* gene (Fig. 3D, lane 5).

Alphafold2 multimer modeling indicated that SpoVK is likely to assume a homo-hexameric functional state comparable to its closest sister clades such as CbbX (Figure S1D). We therefore tested the dominance of the *spoVK* mutant alleles in merodiploid strains that also contained the WT copy of *spoVK*. Co-expressing *spoVK*$^{\Delta NTD}$ or *spoVK*^{A*} did not reduce sporulation efficiency in cells harboring a WT copy of *spoVK* (Fig. 3F, lanes 3-4), presumably because these variants did not accumulate to appreciable levels in the cell. However, co-expression of *spoVK*^{B*} or *spoVK*^{R*} with WT spoVK resulted in 100-1000 fold reduction in sporulation efficiency (Fig. 3F, lanes 5-6). The genetic dominance of these alleles suggested that SpoVK is capable of oligomerizing in vivo and that, similar to other AAA+ proteins, introduction of ATPase-defective subunits can poison the function of the oligomerized chaperone (5).

Finally, we examined if SpoVK could hydrolyze ATP in vitro. Incubation of purified SpoVK-His_6 with increasing concentrations of ATP produced a saturation curve that revealed a substrate turnover rate (k_{cat}) of 104 ± 18 μM released phosphate min^{-1} μM^{-1} SpoVK (Fig. 3G). In contrast, purified SpoVK^{B*} did not appreciably hydrolyze ATP at any of the concentrations tested. Thus, as predicted by the sequence-structure analysis, the *in vivo* and *in vitro* results suggest that SpoVK is a functional AAA+ ATPase.

SpoVK interacts with SpoVID and MurG

To elucidate the role of SpoVK during sporulation, we immunoprecipitated FLAG-tagged SpoVK from sporulating *B. subtilis* cultures and identified co-purifying proteins. To trap associated proteins, we performed the immunoprecipitation with FLAG-tagged SpoVK harboring a disrupted Walker B motif (SpoVK^{B*}-FLAG), a strategy that we have successfully used previously to stabilize interactions between chaperones and potential substrates (36). Immunoprecipitation of SpoVK^{B*}-FLAG from extracts of cells 4 h after induction of sporulation revealed two species specifically in the eluate that were not present when the

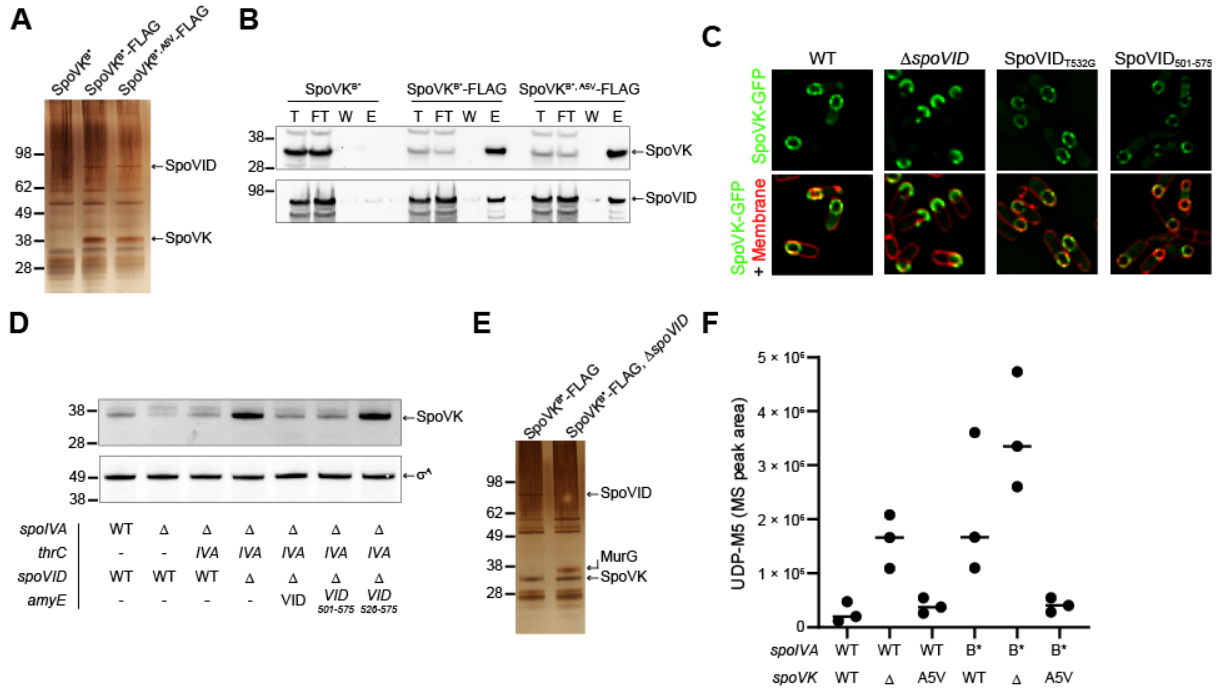

Figure 4. SpoVK interacts with SpoVID and MurG. (A) Silver stain SDS-PAGE of the elution fraction of the SpoVK^{B*}-Flag immunoprecipitation from cells harvested 4 h after the induction of sporulation with anti-FLAG magnetic beads. Strains: TD883, TD884, and TD1193. (B) Immunoblot of Total (T), Flow Through (FT), Wash (W), and Elution (E) of the SpoVK^{B*}-Flag immunoprecipitation from cells harvested 4h after the induction of sporulation with anti-Flag magnetic beads using anti-SpoVK and anti-SpoVID antisera. Strains: TD883, TD884, TD1193. (C) Subcellular localization of SpoVK-GFP in the presence or absence of SpoVID, or in cells producing SpoVID containing a defective LysM domain (T532G), or the SpoVID LysM domain alone (residues 501-575) 3.5 h after the induction of sporulation (Strains TD604, TD651, TD695, and TD1257). (D) Immunoblot of cell extracts of sporulating *B. subtilis* using anti-SpoVK or anti-σ^{A} antisera, from cells harvested at 4h. (Strains: PY79, KP73, KR394, JB171, JB174, TD892, and TD893). (E) Silver stain SDS-PAGE of the elution fraction of the SpoVK^{B*}-Flag immunoprecipitation from Δ*spoVID* cells harvested 4 h after the induction of sporulation with anti-FLAG magnetic beads. Strains TD884 and TD1268. (F) Accumulation of peptidoglycan precursor Park's nucleotide in strains of *B. subtilis* harboring WT (lanes 1-3) or defective (lanes 4-6) alleles of *spoIVA*, in the presence or absence (lanes 2, 5) of *spoVK* or the presence of *spoVK*^{A5V} (lanes 3, 6).

immunoprecipitation was performed with cells producing SpoVK^{B*}-His$_6$: a ~36 kDa band and a ~65 kDa band (Fig. 4A). Trypsin digestion of these bands followed by mass spectrometry revealed, as expected, that the ~36 kDa band was SpoVK^{B*}-FLAG. The ~65 kDa band was identified as SpoVID, a factor that we recently identified as participating in a sporulation checkpoint that monitors spore coat assembly (28). Immunoblotting the fractions using anti-SpoVID antibodies confirmed that SpoVID specifically co-purified with SpoVK^{B*}-FLAG and the gain-of-function SpoVK$^{B*, A5V}$-FLAG, but not SpoVK^{B*}-His$_6$ (Fig. 4B). To test the relationship between SpoVID and SpoVK in vivo, we first examined the subcellular localization of SpoVK-GFP. In the absence of SpoVID, SpoVK-GFP mis-localized on the mother cell-distal side of the

297 forespore instead of uniformly localizing around the entire forespore surface (Fig. 4C). However,
298 this mis-localization of SpoVK did not require the peptidoglycan-binding capability of the SpoVID
299 LysM domain since a single amino acid substitution disrupting this function of the LysM domain
300 (SpoVID^{T532G}) did not result in SpoVK mis-localization (Fig. 4C). Nonetheless, expression of the
301 LysM domain of SpoVID alone (SpoVID$^{501-575}$) was sufficient to restore proper localization of
302 SpoVK-GFP (Fig. 4C), indicating that the C-terminal LysM domain of SpoVID, but not a
303 functional LysM domain (namely, one capable of binding peptidoglycan precursors) *per se*,
304 influences the subcellular localization of SpoVK. We next examined the stability of SpoVK by
305 immunoblotting. In WT cells, SpoVK was detectable at a low level; deletion of *spoIVA*, which
306 results in spore coat mis-assembly, resulted in even lower levels of SpoVK, which was restored
307 upon complementation of *spoIVA* at an ectopic locus (Fig. 4D, lanes 1-3). Deletion of *spoVID*,
308 though, increased the level of SpoVK; this increased level of SpoVK was reversed upon
309 complementation of *spoVID* at an ectopic locus (Fig. 4D, lane 4-5). Expression of the LysM
310 domain of SpoVID alone, as the only copy of SpoVID, was sufficient to maintain low, ~WT levels
311 SpoVK, but additional truncation of the LysM domain resulted in increased levels of SpoVK (Fig.
312 4D, lanes 6-7). We conclude that the LysM domain of SpoVID, which is unmasked when the
313 spore coat fails to assemble properly (28), is simultaneously required for proper localization of
314 SpoVK and negatively influences the stability of SpoVK.

315 To identify other interacting partners for SpoVK, we repeated the immunoprecipitation of
316 SpoVK^{B*}-FLAG, but this time in the absence of SpoVID, which revealed a ~38 kDa co-purifying
317 band that was identified as MurG (Fig. 4E). MurG is the glycosyltransferase that catalyzes the
318 formation of lipid II by transferring the UDP-activated GlcNac to the C4 hydroxyl of MurNAc in
319 lipid I (37). Previously, we had reported that SpoVID sequesters lipid II in response to coat
320 assembly defects. Hence, given the evolutionary affinities of SpoVK (Fig. 3B-C), we wondered if
321 SpoVK was also involved in this pathway, perhaps as a chaperone that regulates MurG activity
322 and thereby the amount of lipid II produced during sporulation. To test this, we examined how

the presence or absence of SpoVK influences the accumulation of the peptidoglycan precursor Park's nucleotide, which is the immediate precursor for lipid I synthesis (the substrate for MurG). In an otherwise WT cell 5.5 h after induction of sporulation, deletion of *spoVK* resulted in increased accumulation of Park's nucleotide, indicating a likely defect in lipid I or lipid II synthesis (Fig. 4F, lanes 1-2). A similar accumulation in Park's nucleotide was not observed in the presence of the *spoVK*^{A5V} (Fig. 4F, lane 3). When coat assembly is impaired by an ATPase-defective SpoIVA (SpoIVA^{B*}) that does not polymerize, we observed an increase in the accumulation of Park's nucleotide, similar to what we observed previously (28). This accumulation was exacerbated in the absence of SpoVK but was corrected in the presence of SpoVK^{A5V} (Fig. 4F, lanes 4-6). In sum, the data thus far are consistent with a model in which SpoVK positively influences MurG to promote cortex assembly. Further, the data suggest that SpoVID, via its C-terminal LysM domain, negatively regulates SpoVK activity, albeit independently of its lipid II-binding function.

The forespore surface is more acidic relative to the mother cell cytoplasm

To test if the negative regulatory activity of the SpoVID LysM domain on SpoVK is via a direct interaction, we immunoprecipitated SpoVK^{B*}-FLAG from cell extracts 4 h after induction of sporulation using cells that also produced GFP fused to the LysM domain of SpoVID (GFP-SpoVID$^{501-575}$). Immunoblotting the fractions using anti-GFP antibodies indicated that GFP-SpoVID$^{501-575}$ specifically co-purified with SpoVK^{B*}-FLAG (Fig. 5A). Since the *spoVK*^{A5V} suppressor mutation mapped to the N-terminal domain, which is predicted to play a role in recruiting the substrate, we next sought to identify which protein binds to the SpoVK N-terminus. We therefore immunoprecipitated a SpoVK^{B*}-FLAG variant in which amino acids 2-5 were deleted (SpoVK$^{\Delta 2-6}$-FLAG) or harbored the A5V suppressor substitution (SpoVK^{A5V}-FLAG) from cell extracts 4 h after induction of sporulation and first monitored the co-purification of SpoVID. Immunoprecipitation of SpoVK $^{\Delta 2-6}$-FLAG or SpoVK-FLAG resulted in similar co-purification of

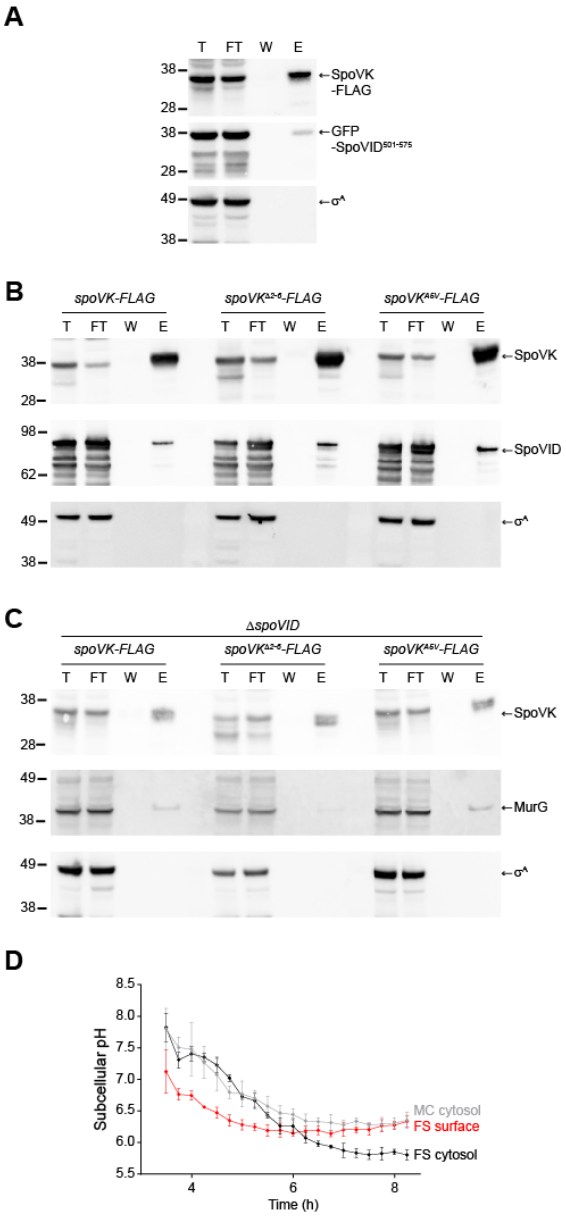

Figure 5. SpoVK interacts with SpoVID and MurG at an acidified forespore surface. (A) Immunoblots of total (T), flow through (FT), wash (W), and elution (E) fractions of the SpoVK^{B*}-Flag immunoprecipitation from cells producing GFP-SpoVID$^{501-575}$ (containing the SpoVID LysM domain) harvested 4h after the induction of sporulation with anti-Flag magnetic beads using anti-SpoVK, anti-GFP, or anti-σ^{A} antisera. Strain: TD1281. (B-C) Immunoblots of fractions described above, of the SpoVK^{B*}-Flag immunoprecipitation (left), SpoVK^{B*}-Flag with residues 2-5 deleted (middle), or SpoVK^{B*}-Flag harboring the A5V substitution from cells that either (B) produce or (C) do not produce SpoVID, using anti-SpoVK, anti-SpoVID, or anti-σ^{A} antisera. Strains: TD1267, TD1277, TD1283, TD1268, TD1278, and TD1284. (D) Subcellular pH measurements in a sporangium near the producing lpHluorin fusions to SpoVM (to measure the forespore surface, "FS surface", red), or free lpHluorin produced in the mother cell cytosol ("MC cytosol", gray), or forespore cytosol ("FS cytosol", black) taken at indicated time points after induction of sporulation. pH values were obtained by measurement of the emission fluorescence at 510 nm after excitation at 390 nm and 470 nm. After obtaining the emission ratio of 390 nm/470 nm, pH was calculated using a calibration curve obtained by growing lpHluorin-producing cells in media of defined pH in the presence of an electrochemical gradient dissipator. Data points represent mean of 4 independent biological replicates; errors are S.D. Strains: SC765, SC767, and SC766.

SpoVID (Fig. 5B), indicating that the N-terminus of SpoVK is not necessary for the interaction of SpoVK with SpoVID. We then repeated the experiment in a strain harboring a deletion of *spoVID*, which increased the interaction of SpoVK with MurG (Fig. 4E). An Alphafold2 multimer model suggested that the N-terminal domain of SpoVK is likely to form part of its interaction interface with MurG (Fig. S1E). Consistent with this, whereas MurG co-purified with SpoVK-FLAG and SpoVK^{A5V}-FLAG, the amount of MurG that co-purified with SpoVK $^{\Delta 2\text{-}6}$-FLAG was diminished (Fig. 5C), indicating that the N-terminus of SpoVK is required for the interaction between SpoVK and MurG. In conclusion, although SpoVID interacts with SpoVK, SpoVID is likely not a substrate for the SpoVK. However, since the interaction of MurG

with SpoVK depends on the N-terminus of SpoVK, we conclude that MurG is likely a substrate of the SpoVK chaperone.

MurG is an essential protein that reportedly does not require activation by a chaperone for normal function (37), so we wondered why it would need to be activated during sporulation. At the onset of sporulation, MurG redeploys from the mother cell membrane to the outer forespore membrane (30). Previously, based on two observations, we speculated that the forespore surface may represent a unique nanoenvironment in the mother cell cytosol. First, the LysM domain of SpoVID displays an unusually low pI (4.8) and is only functional in vitro in acidic buffer conditions (28). Second, SpoIVA, which is among the most abundant proteins on the forespore surface (14), also displays an acidic isoelectric point (4.5). Previous studies have shown that the forespore interior is ultimately acidified compared to the mother cell cytosol, which remains largely at neutral pH (38, 39), but the status of the nanoenvironment immediately atop the developing forespore in the mother cell cytosol is not known. To measure the pH of this region, we fused the pH-sensitive fluorescent protein IpHluorin to SpoVM, a peripheral membrane protein that tethers SpoIVA to the forespore surface (40). As controls, we also measured the pH of the mother cell and forespore cytosol by producing free IpHluorin either under control of a mother cell-specific promoter (P_{spoVM}) or forespore-specific promoter (P_{spoIIQ}). All Iphlorin fusions localized to the expected subcellular location (Fig. S3A-D). At the onset of our measurements, 3.5 h after induction of sporulation, the forespore and mother cell cytosols displayed a similar pH: 7.8 ± 0.33 and 7.8 ± .23, respectively, but the nanoenvironment immediately surrounding the forespore surface displayed a pH of 7.1 ± 0.34. At 4.25 h after induction of sporulation, the overall pH of both the mother cell (7.3 ± 0.3) and forespore (7.4 ± 0.07) cytosols gradually decreased, but remained similar to one another; however, the forespore surface pH was further reduced (6.6 ± 0.02). The relatively lower pH of the forespore surface persisted until 6 h after induction of sporulation, when the forespore cytosol became acidified to a similar extent as the forespore surface. At 8 h after induction of sporulation, the mother cell

386 cytosol (6.35 ± 0.13) was similar to that of the forespore surface (6.33 ± 0.08), whereas the
387 cytosol of the forespore was further acidified (5.8 ± 0.08), as previously reported (38, 39). We
388 therefore conclude that the mother cell cytosol is not uniform and that, even in the absence of
389 membrane-bound compartments, certain patches of the cytosol can exhibit unique chemical and
390 physical properties.
391

DISCUSSION

In non-spherical bacteria such as rods, peptidoglycan assembly at differently shaped regions of the cell (for example, the lateral edge versus the division septum) relies on a shared pool of peptidoglycan precursors in the cytosol that are differently assembled, depending on where on the cell surface the precursors need to be incorporated. The differential utilization of this precursor pool is achieved by specialized complexes (the “divisome” at septa or the “elongasome” for cylindrical growth) that permit the coordination of cell wall synthesis with cell growth.

The sporulation program typically employs factors that are exclusively used for this pathway, even if that requires duplicating an existing gene and modifying it for sporulation (41, 42). Given the precedence of shared peptidoglycan precursor usage for the assembly of different cell wall material, it is interesting that a sporulation-specific peptidoglycan assembly complex has evolved to generate the specialized cortex, which nonetheless utilizes the same pool of peptidoglycan precursors as used for vegetative growth. Indeed, during sporulation, the widely conserved MurG protein, which synthesizes the lipid II precursor, redeploys from the mother cell plasma membrane, where it participates in constructing the vegetative cell wall that surrounds the mother cell, onto the outer forespore membrane during sporulation, where it participates in assembling the cortex surrounding the developing forespore (30). In this study, we propose that the redeployed MurG additionally requires a sporulation-specific chaperone, the previously uncharacterized SpoVK protein, to perform its glycosyltransferase function at the forespore surface. We suggest that this requirement arises from a nanoenvironment immediately surrounding the forespore, which we determined was more acidic than the rest of the mother cell cytosol. The requirement of SpoVK during sporulation also conveniently provides an additional step of regulating cortex assembly. Previously, we demonstrated that cortex assembly is linked to proper initiation of coat assembly by a checkpoint mechanism that actively monitors the polymerization state of the spore coat basement layer: when the coat mis-

418 assembles, cortex assembly is inhibited by sequestration of lipid II by SpoVID (43). However, it
419 was unclear if additional lipid II synthesis would be downregulated in this circumstance to
420 prevent overwhelming this lipid II sequestration mechanism. In our updated model (Fig. 6), we
421 propose that upon sensing a coat assembly defect, SpoVID also inhibits SpoVK by directly
422 binding SpoVK via the LysM domain of SpoVID. Thus, SpoVID prevents the activation of MurG
423 at the forespore surface, resulting in reduced flux of lipid II through the cortex biosynthesis
424 pathway.

425 Our model for how SpoVID controls the coat assembly checkpoint by monitoring SpoIVA
426 polymerization, sequestering lipid II, and modulating the activity of SpoVK is consistent with
427 multiple in vivo and in vitro observations. First, SpoVK co-localizes on the forespore surface with
428 MurG; in the absence of SpoVK, cortex peptidoglycan assembly is diminished and the resulting
429 cell wall surrounding the forespore resembles that resulting from the deletion of other cortex
430 morphogenesis factors (34, 44, 45). Notably, though, while other well-characterized cortex
431 morphogenic proteins localize in the intermembrane space of the forespore, SpoVK is in the
432 mother cell, where it can interact with peptidoglycan precursors, before lipid II is flipped across
433 the outer forespore membrane. Interestingly, the undetectability of SpoVK at an intermediate
434 time point during sporulation that coincides with the completion of cortex assembly and the
435 dehydration of the spore core also suggests that SpoVK plays a defined role in cortex assembly.
436 Second, the evolutionary relationship of SpoVK to the CbbX chaperone, which activates
437 RuBisCo (1), suggests that SpoVK could also act as a comparable chaperone. RuBisCo is a
438 large multimeric complex that is inhibited by its own substrate ribulose 1,5-bisphosphate (RuBP;
439 Fig. 6A). CbbX, in contrast, is stimulated by RuBP, which CbbX binds via the C-terminal four-
440 helical bundle characteristic of AAA+ ATPases. Thus, CbbX captures the C-terminal tail of the
441 RuBisCO large subunit and causes it to release the inhibitor RuBP. Interestingly, MurG has
442 been recently described to also form a large hexameric complex (46). Hence, like RuBisCO, a
443 functional MurG complex might require assistance from a chaperone for assembly/activation in

444

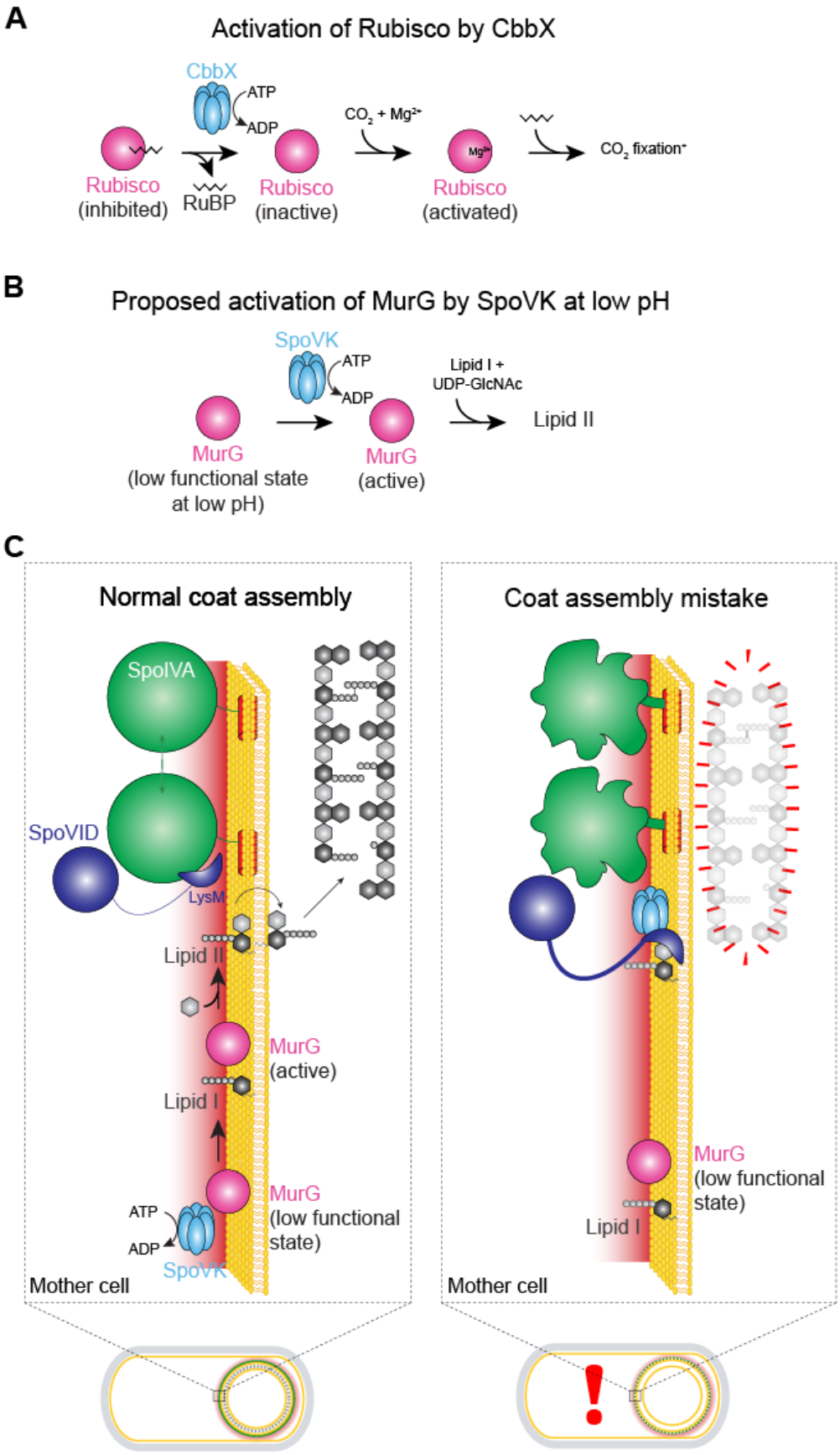

Figure 6. Model for the regulated activation of MurG by SpoVK. (A) Activation of Rubisco, which catalyzes fixation of CO_2 in photosynthesis, by AAA+ chaperone CbbX. Rubisco (pink) forms an inactive complex with its substrate ribulose 1,5-bisphosphate (RuBP, black), which can be reactivated by CbbX (blue). Rubisco is subsequently activated by reacting with CO_2 and Mg^{2+} (adapted from Mueller-Cajar *et al*. (1)). (B) Proposed activation of MurG by AAA+ chaperone SpoVK. MurG exists in a low functional state at the forespore surface due to the low pH in that nanoenvironment. SpoVK, which localizes to the forespore surface, helps fold MurG properly so that it may catalyze the conversion of lipid I to lipid II. (C) Depicted are a sporulating cell of *B. subtilis* that is wild type (left) or a mutant (right) that mis-assembles the spore coat. Expansions of the developing spore envelope (cortex, outer forespore membrane, and coat basement layer) are depicted above each cell. Low pH nanoenvironment is depicted as a red gradient. When SpoIVA (green) polymerizes properly, the LysM domain of SpoVID (purple) is occluded, permitting 1) lipid II to flip to the intermembrane space to incorporate into the assembling cortex and 2) SpoVK (blue) to activate MurG, thereby ensuring a steady flux of lipid II. When SpoIVA mis-assembles (right), the LysM domain of SpoVID is liberated, resulting in 1) sequestration of lipid II and 2) inhibition of SpoVK, resulting in reduced buildup of lipid II in the mother cell cytosol, due to the low functional state of MurG in the forespore surface nanoenvironment.

mutation in the putative substrate binding domain of SpoVK and observed that SpoVK interacts with MurG *in vitro* via this domain. Further, SpoVK shares sequence conservation with CbbX in the C-terminal four-helical bundle which binds the activating carbohydrate RuBP in the latter (Fig. S1B-C). Hence, it would also be of interest to explore if SpoVK might similarly be regulated by soluble carbohydrates such as substrates of MurG. Finally, we found that SpoVK is antagonized by SpoVID, likely by destabilization and that the C-terminal LysM domain of SpoVID, which stably interacts with SpoVK, is sufficient for this antagonism. Thus, detecting improper assembly of the spore coat, sequestering the lipid II peptidoglycan precursor, and reducing the further synthesis of lipid II is mediated by SpoVID, the central factor in the spore coat assembly checkpoint, that interacts with SpoIVA, SpoVK, and lipid II via a single domain.

Our findings have implications for the specific clade of AAA+ domains to which SpoVK belongs that was previously both poorly defined and understudied. The sporulation-specific interaction of SpoVK and MurG adds to the previous evidence from CbbX and EccA that members of this clade are dedicated chaperones that act narrowly on specific targets and/or in specific sub-cellular locations. Indeed, while most well-characterized members of the Classical AAA+ assemblage show fusions or direct physical interaction with diverse peptidase domains, we found no evidence for such associations in this clade. Instead, they typically show a diversity of N-terminal domains which might help recruit distinct substrates to an otherwise well-

463 conserved AAA+ domain. Thus, rather than aiding protein degradation through unfolding, these
464 chaperones might aid macromolecular assembly and activation in several as yet unstudied
465 contexts. Interestingly, in addition to its role in secretion via T7SS, the mycobacterial EccA
466 protein EccA1 has also been shown to be necessary for production of mycolic acids, key
467 component of the actinobacterial cell envelope lipid. This role of EccA1 has been proposed to
468 operate via potential chaperone action on several mycolic acid biosynthesis enzymes (47).
469 Thus, multiple members of this clade might regulate cell envelope composition by acting on the
470 cytosolic enzymes needed for their synthesis.

471 Despite the diminutive size of the cytoplasm of most bacteria, the subcellular
472 organization of macromolecules in this compartment has become increasingly evident in the last
473 several decades (48). Interestingly, our studies in understanding a bacterial developmental
474 checkpoint led us to appreciate that cytosolic compartmentalization may also exist at a chemical
475 level in the form of varying pH, which can necessitate specialized chaperones at distinct regions
476 to carry out cellular functions. More generally, this raises the interesting possibility that the
477 cytoplasm may not be uniform with respect to other chemical properties, such as ionic strength
478 or oxidation state, as well. Perhaps discovering the subcellular localization of chaperones in
479 other systems may highlight other sub-cytosolic locations that harbor chemically distinct regions.
480

ACKNOWLEDGEMENTS

We thank members of the KSR lab for suggestions and comments on the manuscript; S. Gottesman, S. Wickner, A. Khare, T. Bauer, and M. Maurizi for discussions; J. Barriga for strains; F. Soheilian and C. Burks (CCR) for TEM sample preparation and imaging; and the CCR Genomics Core Facility for whole genome sequencing. This work was funded by the National Institutes of Health (NIH) grant R01GM138630 (D.L.P.), the Swedish Research Council, the Laboratory of Molecular Infection Medicine Sweden (MIMS), Umeå University, the Knut and Alice Wallenberg Foundation (KAW), the Kempe Foundation (F.C.), the Intramural Research Program of the NIH, the National Cancer Institute, the Center for Cancer Research (K.S.R.), and the National Library of Medicine (L.A.). This work utilized the NIH HPC Biowulf computer cluster (V.A. and L.A.).

EXPERIMENTAL PROCEDURES

Strain construction

Strains are otherwise isogenic derivatives of *B. subtilis* PY79 (49). Genes of interest were PCR amplified to include their native promoter and cloned into integration vectors pDG1662 (for insertion into the *amyE* locus), pDG1731(*thrC* locus), pSac-Cm (*sacA* locus), or pPyr-Cm (*pyrD* locus) (50, 51). Site-directed mutagenesis was performed using the QuikChange kit (Agilent). For pH measurements, 500 bp upstream of *spoIIQ* or *spoVM* genes were cloned upstream of *Iphluorin* and cloned into pDG1662 (51) to drive production of free Iphluorin in the forespore or mother cell cytosol, respectively. Alternatively, the spoVM ORF, downstream of its native promoter, was fused to *Iphluorin* (52) and cloned into pDG1662 to drive production of membrane-bound SpoVM-Iphluorin. Finally, IPTG-inducible *Iphluorin* was constructed by cloning Iphluorin into vector pDP150 (53). Resulting plasmids were integrated into the specified ectopic locus in the *B. subtilis* chromosome by double recombination.

General methods

Sporulation efficiencies were calculated by growing cells in Difco Sporulation Medium (KD Medical) for at least 24 h. Nonsporulating cells and defective spores were killed by exposure to 80 ºC for 20 min. Heat-killed cultures were serially diluted and colony forming units (cfu) of surviving cells were enumerated and reported relative to cfu enumerated in a parallel culture of WT (PY79) strain. To obtain spontaneous suppressor mutants, strain JPC221 (which harbors the *spoIVA*^{T}* allele as the only copy of *spoIVA* and is unable to sporulate efficiently) was subjected to multiple rounds of growth and heat treatment in DSM to enrich for colonies that displayed increased heat resistance. The suppressor mutation was identified using whole genome sequencing as described previously (28). SpoVK, σ^{A}, SpoVID, GFP, and MurG levels were by immunoblotting cell extracts prepared as described previously (36) using rabbit antiserum raised against recombinant, purified SpoVK-His_6, σ^{A}-His_6, SpoVID-His_6, GFP-His_6,

519 and MurG-His_6 (Covance) as primary antibody and goat Starbright Blue 700 (Bio-Rad) as
520 secondary antibody.
521
522 *Sequence Analysis*
523 Sequence similarity searches were performed using the PSI-BLAST program with a profile-
524 inclusion threshold set at an e-value of 0.01 (54). The searches were conducted against the
525 NCBI non-redundant (nr) database, or the same database clustered down to 50% sequence
526 identity using the MMseqs program, or a curated database of 7423 representative genomes
527 from across the tree of life. Profile-profile searches were performed with the HHpred program
528 (55, 56). Multiple sequence alignments (MSAs) were constructed using the FAMSA and MAFFT
529 programs (57, 58). Sequence logos were constructed using these alignments with the
530 ggseqlogo library for the R language (59).
531
532 *Structure Analysis*
533 PDB coordinates of structures were retrieved from the Protein Data Bank and structures were
534 rendered, compared, and superimposed using the Mol* program (60). Structural models were
535 generated using the AlphaFold2 and AlphaFold-Multimer programs (61, 62). Multiple alignments
536 of related sequences (>30% similarity) were used to initiate HHpred searches for the step of
537 identifying templates to be used by the neural networks deployed by these programs.
538
539 *Comparative Genomics and Phylogenetic Analysis*
540 Clustering of protein sequences and the subsequent assignment of sequences to distinct
541 families was performed by the MMseqs program (63), adjusting the length of aligned regions
542 and bit-score density threshold empirically. Phylogenetic analysis was performed using the
543 maximum-likelihood method with the IQTree program (64) and multiple protein substitution
544 models such as Dayhoff, Poisson, and JTTMutDC. The FigTree program

(http://tree.bio.ed.ac.uk/software/figtree/) was used to render phylogenetic trees. Gene neighborhoods were extracted through custom PERL scripts from genomes retrieved from the NCBI Genome database.

Epifluorescence microscopy

B. subtilis cells were induced to sporulate by the resuspension method in SM medium (65). At indicated time points, 100 µl of culture was harvested and resuspended in 10 µl SM containing 5 µg ml^{-1} FM4-64 fluorescent dye to visualize membranes. Resuspensions were then placed on a glass-bottom culture dish (MatTek) and covered with a 1% agarose pad made with SM. Cells were viewed at room temperature with a DeltaVision Core microscope system (Applied Precision/GE Healthcare). Seven planes were acquired every 200 nm and the data were deconvolved using SoftWorx software as described previously (66). Additional image adjustments were performed using Fiji software.

Transmission electron microscopy

B. subtilis cells were induced to sporulate by resuspension in SM for the indicated time period (> 24 h for mature spores), harvested by centrifugation, washed with water, and fixed in 4% formaldehyde and 2% glutaraldehyde in 0.1 M cacodylate buffer, post fixed using a 1% osmium tetroxide solution, then dehydrated sequentially in 35%, 50%, 75%, 95% and 100% ethanol followed by 100% propylene oxide. Cells were infiltrated in an equal volume of 100% propylene oxide and epoxy resin overnight and embedded in pure resin the following day. The epoxy resin was cured at 55 °C for 48 h. The cured block was thin-sectioned and stained in uranyl acetate and lead citrate. The sample was imaged with a Hitachi H7600 TEM equipped with a CCD camera (67).

SpoVK purification

SpoVK-His_6 was purified by affinity chromatography under denaturing conditions and renatured. Overnight cultures of *E. coli* strains BL21(DE3) pTD211 (expressing *spoVK-His_6*) or pTD308 (expressing *$spoVK^{D162A,E163A}$-His_6*) in LB containing 50 µg ml^{-1} kanamycin for plasmid maintenance were diluted 1:100 into 500 ml LB/kanamycin and grown at 37 ºC shaking at 250 rpm for 2 h. Isopropyl thiogalactopyranoside was then added at 1 mM final concentration to induce protein production and cells were grown for a further 3 h. Cells were harvested by centrifugation and cell pellets were stored at -80 ºC. Cell pellets were resuspended in lysis buffer (100 mM sodium phosphate, 10 mM Tris-HCl, 8 M Urea at a final pH of 7.5) and disrupted in a French pressure cell at ca. 20,000 psi. Insoluble material was removed by centrifugation at ~100,000 × g, and the supernatant was applied onto a 1.5 ml (bed volume) Ni^{2+}-NTA agarose column equilibrated with lysis buffer. The column was washed with 30 ml of lysis buffer and eluted with 4 ml lysis buffer containing 250 mM imidazole. 3 ml of purified SpoVK-His_6 was then dialyzed once overnight against 500 ml renaturation buffer (500 mM L-arginine, 100 mM NaCl at pH 7.5) using a 10 kDa MWCO membrane. Dialyzed sample was then collected, and insoluble material was removed by centrifugation at ~15,000 × g for 5 min at 4 ºC. 500 µl of the supernatant was then applied to a Superdex 200 Increase size exclusion chromatography column (Cytiva) and separated using renaturation buffer using flow rate of 0.75 ml min^{-1}. The final peak, corresponding to an approximate trimer of SpoVK, was used for analysis.

Co-immunoprecipitation

B. subtilis cells were induced to sporulate by resuspension in 15 ml SM for 4 h, and cell pellets harvested by centrifugation were stored at -80 ºC. Pellets were resuspended in 1 ml protoplast buffer (0.5 M sucrose, 20 mM $MgCl_2$, 10 mM potassium phosphate at pH 6.8, 1 mg/ml lysozyme) and incubated at 37 ºC for 25 min to generate protoplasts. Protoplasts were harvested by centrifugation and resuspended in 1 ml binding buffer (50 mM Tris-HCl at pH 7.5, 150 mM NaCl, 7.5% glycerol, 0.2% Triton-X-100). Cell debris was removed by centrifugation at

~15,000 × g, and the supernatant was combined with an additional 150 µl of binding buffer and added to 50 µl magnetic agarose beads (Pierce) equilibrated with binding buffer and incubated at 4 ºC for 1 h. Beads were washed thrice with 1 ml of binding buffer and eluted with 100 mM glycine at pH 2.7.

Preparation and analysis of forespore peptidoglycan

Cortex peptidoglycan was prepared and analyzed as previously described (68). Briefly, 50 ml cultures were induced to sporulate by resuspension as described above. 5 h after induction of sporulation, cells were harvested by centrifugation and pelleted cells were resuspended in 5 ml SMM protoplast solution (0.5 M sucrose, 20 mM Maleic Acid, 20 mM $MgCl_2$) containing 25 mg/ml lysozyme to digest mother cell peptidoglycan and incubated at 37 ºC for 15 min. 45 ml boiling lysis buffer (4% sodium dodecyl sulfate, 50 mM dithiothreitol) was then added to the resulting protoplasts and boiled for 20 min. After cooling to room temperature, insoluble material was collected by centrifugation at 21,000 × g for 30 min and resuspended in 1 ml water, boiled for 5 min to solubilize residual SDS, then centrifuged at 21,000 × g for 20 min to collect insoluble material. Washes were repeated until no SDS was detected. Resuspended material in 1 ml buffer (100 mM Tris at pH 7.0, 20 mM $MgSO_4$) were treated with 10 µg/ml DNase I and 50 µg/ml RNase A for 2h at 37 ºC. 100 µg trypsin and 10 mM $CaCl_2$ were added and the sample was incubated at 37 °C for 16 h. Insoluble material was collected by centrifugation at 21,000 × g for 20 min, resuspended in 1 ml 1% SDS, and boiled for 20 min to inactivate trypsin. Samples were washed with water as described above and isolated spore peptidoglycan was digested with 125 U of Mutanolysin in a total volume of 250 µl of 12.5 mM $NaPO_4$ at pH 5.5 for 16 h at 37 °C. Solubilized muropeptides were separated by reverse phase HPLC as described previously (69).

Peptidoglycan accumulation

Quantification of Park's nucleotide was performed as described previously (28). Briefly, cells were induced to sporulate by resuspension in SM, harvested at t = 5.5 h, and washed thrice with ice cold 0.9% NaCl, resuspended in a final volume of 100 µl 0.9% NaCl, and boiled for 5 min to extract soluble peptidoglycan precursors. Insoluble material was pelleted by centrifugation at 21,000 × g for 5 min and the resulting supernatant was filtered through a 0.22 µm pore-size filter. Detection and quantification of Park's nucleotide was performed by LC-MS analysis using a UPLC system (Waters) equipped with an ACQUITY UPLC BEH C18 column (130Å pore size, 1.7 µm particle size, 2.1 mm x 150 mm, Waters) coupled to a Xevo G2-XS QTOF mass spectrometer (Waters). Chromatographic separation of the soluble fraction was achieved using a linear gradient from 0.1% formic acid in water to 0.1% formic acid in acetonitrile over 18 min at 45 °C. The QTOF instrument was operated in positive ionisation mode and detection of UDP-M5 was performed in the untargeted MS^e mode. The MS parameters were set as follows: capillary voltage 3 kV, source temperature 120 °C, desolvation temperature 350 °C, sample cone voltage 40 V, cone gas flow 100 L h^{-1}, and desolvation gas flow 500 L h^{-1}. Data acquisition and processing was performed using the UNIFI software (Waters). To quantify the Park's nucleotide, its calculated $[M+2H]^{2+}$ ion of *m/z* 597.68 was extracted from the total ion chromatogram, and the corresponding peak in the resulting extracted ion chromatogram was integrated to give a peak area.

ATP hydrolysis assay

ATP hydrolysis was measured as previously described (16). Briefly, varying concentrations of ATP were incubated with 1 µM purified SpoVK-His_6 or $SpoVK^{B*}$-His_6 in 100 µl of buffer (500 mM L-arginine at pH 7.5, 100 mM NaCl, 5 mM $MgCl_2$) for 20 min at 37 ºC. Concentration of inorganic phosphate was determined using the Malachite Green Phosphate Assay kit (BioAssay Systems) according to manufacturer's protocol. Absorbance at 620 nm (Spark 10M plate reader, Tecan) of each reaction was compared to absorbances of known concentrations of

649 phosphate standards. Absorbances from control reactions performed in the absence of SpoVK
650 for each ATP concentration were subtracted from absorbances of the respective reactions with
651 SpoVK to eliminate background hydrolysis. For each ATP concentration, hydrolysis rates were
652 plotted using GraphPad Prism 7; V_{max} and K_m values were determined by fitting the data to
653 Michaelis–Menten equation using best-fit values.
654
655 *Intracellular pH measurements*
656 Strains SC765, SC766, and SC767 were induced to sporulate by the resuspension method as
657 described above. 200 µl of each culture were then placed into individual wells of black-walled
658 96-well plates and placed in a Synergy H1 plate reader (BioTek) and grown at 37 ºC, with
659 continuous shaking. Fluorescence signal (emission at 510 nm, with excitation at 390 nm and
660 470 nm) was measured every 15 min and the 390/470 ratios were calculated. To convert the
661 390/470 ratios to pH values, we constructed a calibration curve as described previously (39)
662 (Fig. S3E). Briefly, strain SC777, which produces IPTG-inducible Iphluorin, was grown in
663 casein-hydrolysate (CH) medium with 1 mM IPTG, then induced to sporulate by resuspension in
664 Sterlini-Mandelstam medium (65) containing 10 mM Tris at pH 7.5, 1 µM nigericin, and 1 µM
665 valinomycin (to equilibrate external and internal pH) that was adjusted to different pH values
666 ranging from 5 to 8.5 using 5N NaOH or 6N HCl. Fluorescence signals of cells grown at different
667 pH values were measured as described above, and 390/470 ratios were calculated and plotted
668 as a function of pH. The resulting plot was fit with a linear curve with equation y = 0.7868x –
669 2.638, where y represents 390/470 ratio and x represents pH.
670

REFERENCES

1. O. Mueller-Cajar *et al.*, Structure and function of the AAA+ protein CbbX, a red-type Rubisco activase. *Nature* **479**, 194-199 (2011).
2. S. Wickner, T. L. Nguyen, O. Genest, The Bacterial Hsp90 Chaperone: Cellular Functions and Mechanism of Action. *Annu Rev Microbiol* **75**, 719-739 (2021).
3. A. Alam, J. E. Broms, R. Kumar, A. Sjostedt, The Role of ClpB in Bacterial Stress Responses and Virulence. *Front Mol Biosci* **8**, 668910 (2021).
4. M. Hayer-Hartl, A. Bracher, F. U. Hartl, The GroEL-GroES Chaperonin Machine: A Nano-Cage for Protein Folding. *Trends Biochem Sci* **41**, 62-76 (2016).
5. T. V. Seraphim, W. A. Houry, AAA+ proteins. *Curr Biol* **30**, R251-R257 (2020).
6. L. M. Iyer, D. D. Leipe, E. V. Koonin, L. Aravind, Evolutionary history and higher order classification of AAA+ ATPases. *J Struct Biol* **146**, 11-31 (2004).
7. A. F. Neuwald, L. Aravind, J. L. Spouge, E. V. Koonin, AAA+: A class of chaperone-like ATPases associated with the assembly, operation, and disassembly of protein complexes. *Genome Res* **9**, 27-43 (1999).
8. E. P. Riley, C. Schwarz, A. I. Derman, J. Lopez-Garrido, Milestones in Bacillus subtilis sporulation research. *Microb Cell* **8**, 1-16 (2020).
9. A. Shen, A. N. Edwards, M. R. Sarker, D. Paredes-Sabja, Sporulation and Germination in Clostridial Pathogens. *Microbiol Spectr* **7** (2019).
10. I. S. Tan, K. S. Ramamurthi, Spore formation in Bacillus subtilis. *Environ Microbiol Rep* **6**, 212-225 (2014).
11. P. T. McKenney, A. Driks, P. Eichenberger, The Bacillus subtilis endospore: assembly and functions of the multilayered coat. *Nat Rev Microbiol* **11**, 33-44 (2013).
12. K. D. Price, R. Losick, A four-dimensional view of assembly of a morphogenetic protein during sporulation in Bacillus subtilis. *J Bacteriol* **181**, 781-790 (1999).

13. I. L. Wu *et al.*, A versatile nano display platform from bacterial spore coat proteins. *Nat Commun* **6**, 6777 (2015).

14. E. A. Peluso, T. B. Updegrove, J. Chen, H. Shroff, K. S. Ramamurthi, A 2-dimensional ratchet model describes assembly initiation of a specialized bacterial cell surface. *Proc Natl Acad Sci U S A* **116**, 21789-21799 (2019).

15. K. S. Ramamurthi, R. Losick, ATP-driven self-assembly of a morphogenetic protein in Bacillus subtilis. *Mol Cell* **31**, 406-414 (2008).

16. T. B. Updegrove *et al.*, Reformulation of an extant ATPase active site to mimic ancestral GTPase activity reveals a nucleotide base requirement for function. *Elife* **10** (2021).

17. J. P. Castaing, A. Nagy, V. Anantharaman, L. Aravind, K. S. Ramamurthi, ATP hydrolysis by a domain related to translation factor GTPases drives polymerization of a static bacterial morphogenetic protein. *Proc Natl Acad Sci U S A* **110**, E151-160 (2013).

18. D. L. Popham, C. B. Bernhards, Spore Peptidoglycan. *Microbiol Spectr* **3** (2015).

19. P. D. A. Rohs, T. G. Bernhardt, Growth and Division of the Peptidoglycan Matrix. *Annu Rev Microbiol* **75**, 315-336 (2021).

20. R. McQuillen, J. Xiao, Insights into the Structure, Function, and Dynamics of the Bacterial Cytokinetic FtsZ-Ring. *Annu Rev Biophys* **49**, 309-341 (2020).

21. T. Do, J. E. Page, S. Walker, Uncovering the activities, biological roles, and regulation of bacterial cell wall hydrolases and tailoring enzymes. *J Biol Chem* **295**, 3347-3361 (2020).

22. J. G. Coote, Sporulation in Bacillus subtilis. Characterization of oligosporogenous mutants and comparison of their phenotypes with those of asporogenous mutants. *J Gen Microbiol* **71**, 1-15 (1972).

23. Y. Imae, J. L. Strominger, Cortex content of asporogenous mutants of Bacillus subtilis. *J Bacteriol* **126**, 914-918 (1976).

24. P. J. Piggot, J. G. Coote, Genetic aspects of bacterial endospore formation. *Bacteriol Rev* **40**, 908-962 (1976).

25. F. Nunes *et al.*, SpoVID functions as a non-competitive hub that connects the modules for assembly of the inner and outer spore coat layers in Bacillus subtilis. *Mol Microbiol* **110**, 576-595 (2018).

26. K. H. Wang *et al.*, The coat morphogenetic protein SpoVID is necessary for spore encasement in Bacillus subtilis. *Mol Microbiol* **74**, 634-649 (2009).

27. D. Mullerova, D. Krajcikova, I. Barak, Interactions between Bacillus subtilis early spore coat morphogenetic proteins. *FEMS Microbiol Lett* **299**, 74-85 (2009).

28. T. Delerue *et al.*, Bacterial developmental checkpoint that directly monitors cell surface morphogenesis. *Dev Cell* **57**, 344-360 e346 (2022).

29. N. Fan, S. Cutting, R. Losick, Characterization of the Bacillus subtilis sporulation gene spoVK. *J Bacteriol* **174**, 1053-1054 (1992).

30. S. M. Gifford, P. Meyer, Enzyme function is regulated by its localization. *Comput Biol Chem* **59 Pt B**, 113-122 (2015).

31. S. Roels, A. Driks, R. Losick, Characterization of spoIVA, a sporulation gene involved in coat morphogenesis in Bacillus subtilis. *J Bacteriol* **174**, 575-585 (1992).

32. D. Foulger, J. Errington, Sequential activation of dual promoters by different sigma factors maintains spoVJ expression during successive developmental stages of Bacillus subtilis. *Mol Microbiol* **5**, 1363-1373 (1991).

33. J. P. Castaing *et al.*, An autoinhibitory conformation of the Bacillus subtilis spore coat protein SpoIVA prevents its premature ATP-independent aggregation. *FEMS Microbiol Lett* **358**, 145-153 (2014).

34. P. Vasudevan, A. Weaver, E. D. Reichert, S. D. Linnstaedt, D. L. Popham, Spore cortex formation in Bacillus subtilis is regulated by accumulation of peptidoglycan precursors under the control of sigma K. *Mol Microbiol* **65**, 1582-1594 (2007).

35. T. D. Crosskey, K. S. H. Beckham, M. Wilmanns, The ATPases of the mycobacterial type VII secretion system: Structural and mechanistic insights into secretion. *Prog Biophys Mol Biol* **152**, 25-34 (2020).

36. I. S. Tan, C. A. Weiss, D. L. Popham, K. S. Ramamurthi, A Quality-Control Mechanism Removes Unfit Cells from a Population of Sporulating Bacteria. *Dev Cell* **34**, 682-693 (2015).

37. S. Ha, B. Gross, S. Walker, E. Coli MurG: a paradigm for a superfamily of glycosyltransferases. *Curr Drug Targets Infect Disord* **1**, 201-213 (2001).

38. N. G. Magill, A. E. Cowan, D. E. Koppel, P. Setlow, The internal pH of the forespore compartment of Bacillus megaterium decreases by about 1 pH unit during sporulation. *J Bacteriol* **176**, 2252-2258 (1994).

39. J. W. van Beilen, S. Brul, Compartment-specific pH monitoring in Bacillus subtilis using fluorescent sensor proteins: a tool to analyze the antibacterial effect of weak organic acids. *Front Microbiol* **4**, 157 (2013).

40. K. S. Ramamurthi, Protein localization by recognition of membrane curvature. *Curr Opin Microbiol* **13**, 753-757 (2010).

41. H. Chan, A. M. T. Mohamed, I. Grainge, C. D. A. Rodrigues, FtsK and SpoIIIE, coordinators of chromosome segregation and envelope remodeling in bacteria. *Trends Microbiol* **30**, 480-494 (2022).

42. M. Y. Galperin, N. Yutin, Y. I. Wolf, R. Vera Alvarez, E. V. Koonin, Conservation and Evolution of the Sporulation Gene Set in Diverse Members of the Firmicutes. *J Bacteriol* **204**, e0007922 (2022).

43. T. Delerue, K. S. Ramamurthi, How bacteria block their own biofilms. *J Biol Chem* **296**, 100392 (2021).

44. A. Fay, P. Meyer, J. Dworkin, Interactions between late-acting proteins required for peptidoglycan synthesis during sporulation. *J Mol Biol* **399**, 547-561 (2010).

45. E. Bukowska-Faniband, L. Hederstedt, Cortex synthesis during Bacillus subtilis sporulation depends on the transpeptidase activity of SpoVD. *FEMS Microbiol Lett* **346**, 65-72 (2013).

46. K. H. Jung, S. Kwon, C. M. Kim, J. H. Lee, H. H. Park, Putative hexameric glycosyltransferase functional unit revealed by the crystal structure of Acinetobacter baumannii MurG. *IUCrJ* **8**, 574-583 (2021).

47. S. A. Joshi *et al.*, EccA1, a component of the Mycobacterium marinum ESX-1 protein virulence factor secretion pathway, regulates mycolic acid lipid synthesis. *Chem Biol* **19**, 372-380 (2012).

48. L. Shapiro, H. H. McAdams, R. Losick, Why and how bacteria localize proteins. *Science* **326**, 1225-1228 (2009).

49. P. Youngman, J. B. Perkins, R. Losick, Construction of a cloning site near one end of Tn917 into which foreign DNA may be inserted without affecting transposition in Bacillus subtilis or expression of the transposon-borne erm gene. *Plasmid* **12**, 1-9 (1984).

50. R. Middleton, A. Hofmeister, New shuttle vectors for ectopic insertion of genes into Bacillus subtilis. *Plasmid* **51**, 238-245 (2004).

51. A. M. Guerout-Fleury, N. Frandsen, P. Stragier, Plasmids for ectopic integration in Bacillus subtilis. *Gene* **180**, 57-61 (1996).

52. G. Miesenbock, D. A. De Angelis, J. E. Rothman, Visualizing secretion and synaptic transmission with pH-sensitive green fluorescent proteins. *Nature* **394**, 192-195 (1998).

53. D. B. Kearns, R. Losick, Cell population heterogeneity during growth of Bacillus subtilis. *Genes Dev* **19**, 3083-3094 (2005).

54. A. A. Schaffer *et al.*, Improving the accuracy of PSI-BLAST protein database searches with composition-based statistics and other refinements. *Nucleic Acids Res* **29**, 2994-3005 (2001).

55. J. Soding, Protein homology detection by HMM-HMM comparison. *Bioinformatics* **21**, 951-960 (2005).

56. J. Soding, A. Biegert, A. N. Lupas, The HHpred interactive server for protein homology detection and structure prediction. *Nucleic Acids Res* **33**, W244-248 (2005).

57. K. Katoh, J. Rozewicki, K. D. Yamada, MAFFT online service: multiple sequence alignment, interactive sequence choice and visualization. *Brief Bioinform* **20**, 1160-1166 (2019).

58. S. Deorowicz, A. Debudaj-Grabysz, A. Gudys, FAMSA: Fast and accurate multiple sequence alignment of huge protein families. *Sci Rep* **6**, 33964 (2016).

59. O. Wagih, ggseqlogo: a versatile R package for drawing sequence logos. *Bioinformatics* **33**, 3645-3647 (2017).

60. D. Sehnal *et al.*, Mol* Viewer: modern web app for 3D visualization and analysis of large biomolecular structures. *Nucleic Acids Res* **49**, W431-W437 (2021).

61. J. Jumper *et al.*, Highly accurate protein structure prediction with AlphaFold. *Nature* **596**, 583-589 (2021).

62. R. Evans *et al.*, Protein complex prediction with AlphaFold-Multimer. *bioRxiv* 10.1101/2021.10.04.463034 (2022).

63. M. Mirdita, M. Steinegger, J. Soding, MMseqs2 desktop and local web server app for fast, interactive sequence searches. *Bioinformatics* **35**, 2856-2858 (2019).

64. B. Q. Minh *et al.*, IQ-TREE 2: New Models and Efficient Methods for Phylogenetic Inference in the Genomic Era. *Mol Biol Evol* **37**, 1530-1534 (2020).

65. J. M. Sterlini, J. Mandelstam, Commitment to sporulation in Bacillus subtilis and its relationship to development of actinomycin resistance. *Biochem J* **113**, 29-37 (1969).

66. P. J. Eswara *et al.*, An essential Staphylococcus aureus cell division protein directly regulates FtsZ dynamics. *Elife* **7** (2018).

67. S. E. Ebmeier, I. S. Tan, K. R. Clapham, K. S. Ramamurthi, Small proteins link coat and cortex assembly during sporulation in Bacillus subtilis. *Mol Microbiol* **84**, 682-696 (2012).

68. J. Meador-Parton, D. L. Popham, Structural analysis of Bacillus subtilis spore peptidoglycan during sporulation. *J Bacteriol* **182**, 4491-4499 (2000).

69. D. L. Popham, J. Helin, C. E. Costello, P. Setlow, Analysis of the peptidoglycan structure of Bacillus subtilis endospores. *J Bacteriol* **178**, 6451-6458 (1996).

SUPPORTING INFORMATION

Table S1. Cortex peptidoglycan analysis of WT and Δ*spoVK* strains. Extracted peptidoglycan from developing forespores of the wild type and Δ*spoVK* strains harvested 5 h after the onset of sporulation was digested with mutanolysin and separated using HPLC. Muropeptides were identified based on previous studies of elution times[1,2]. Peaks were then integrated, and peptidoglycan structural parameters were calculated. Errors are S.D.

PG species	WT	Δ*spoVK*
% muramic acid as lactam	33.3 ± 1.5	6.5 ± 3.0
% muramic acid with alanine	20.6 ± 0.6	19.5 ± 0.9
% muramic acid with tripeptide	15.9 ±1.9	42.9 ± 3.7
% muramic acid with tetrapeptide	30.2 ± 0.4	31.2 ± 1.4
% muramic acid with pentapeptide	0.0 ± 0.0	0.0 ± 0.0
% peptide as tetrapeptide	65.6 ± 3.0	42.2 ± 2.5
% peptide as tripeptide	34.4 ± 3.0	57.8 ± 2.5
% peptide in crosslinks	19.0 ± 0.6	20.4 ± 2.2
% peptide in effective crosslinks	19.0 ± 0.6	20.4 ± 2.2
% disaccharide units in disaccharides	36.4 ± 3.0	87.1 ± 6.0
% disaccharide units in tetrasaccharides	54.7 ± 2.8	12.9 ± 6.0
% disaccharide units in hexasaccharides	9.0 ± 0.5	0.0 ± 0.0
% lactam in regular distribution	82.1 0.9	100.0 ± 0.0
% disaccharide peptide crosslinked	23.8 ± 0.3	20.4 ± 2.2
% tetrasaccharide peptide crosslinked	5.0 ± 0.2	0.0 ± 0.0
% lactam reduced	0.2 ± 0.0	0.2 ± 0.0
% tripeptide crosslinked	39.6 ± 0.8	31.1 ± 1.7
% tetrapeptide crosslinked	8.2 ± 0.5	5.7 ± 4.7
% disaccharide per effective crosslink	11.5 ± 0.7	6.6 ± 0.4
% muramic acid with crosslink	8.8 ± 0.5	15.1 ± 0.9

[1]DOI: 10.1128/JB.182.16.4491-4499.2000
[2]DOI: 10.1128/jb.178.22.6451-6458.1996

Table S2. Bacterial Strains.

Bacillus subtilis strains used in this study		
Strain	Genotype or description	Reference
PY79	Prototrophic derivative of *B. subtilis* 168	Youngman et al., 1984
KP73	Δ*spoIVA::neo*	Price and Losick, 1999
KR160	*thrC::gfp-spoIVA spec*	Ramamurthi and Losick, 2008
TD549	Δ*spoVK::erm thrC::gfp-spoIVA spec*	This study
TD520	Δ*spoVK::erm*	This study
TD513	Δ*spoVK::erm amyE::spoVK cat*	This study
TD514	Δ*spoVK::erm amyE::spoVK^{A5V} cat*	This study
JPC221	Δ*spoIVA::neo thrC::spoIVA^{T70A,T71A} spec*	Castaing et al., 2013
TD524	Δ*spoIVA::neo thrC:: spoIVA^{T70A,T71A} spec* Δ*spoVK::erm*	This study
TD530	Δ*spoIVA::neo thrC:: spoIVA^{T70A,T71A} spec* Δ*spoVK::erm amyE::spoVK cat*	This study
TD531	Δ*spoIVA::neo thrC:: spoIVA^{T70A,T71A} spec* Δ*spoVK::erm amyE::spoVK^{A5V} cat*	This study
TD523	Δ*spoIVA::neo thrC::spoIVA^{D97A} spec* Δ*spoVK::erm*	This study
TD528	Δ*spoIVA::neo thrC::spoIVA^{D97A} spec* Δ*spoVK::erm amyE::spoVK cat*	This study
TD529	Δ*spoIVA::neo thrC::spoIVA^{D97A} spec* Δ*spoVK::erm amyE::spoVK^{A5V} cat*	This study
KR438	Δ*spoIVA::neo thrC::spoIVA^{K30E} spec*	Ramamurthi and Losick, 2008
TD817	Δ*spoIVA::neo thrC::spoIVA^{K30E} spec* Δ*spoVK::erm*	This study
TD818	Δ*spoIVA::neo thrC::spoIVA^{K30E} spec* Δ*spoVK::erm amyE::spoVK cat*	This study
TD819	Δ*spoIVA::neo thrC::spoIVA^{K30E} spec* Δ*spoVK::erm amyE::spoVK^{A5V} cat*	This study
TD845	Δ*spoIVA::neo amyE::spoIVA^{D97A} cat thrC::GFP-spoIVA^{D97A} spec* Δ*spoVK::erm pyrD::spoVK cat::tet*	This study
TD846	Δ*spoIVA::neo amyE::spoIVA^{T70A,T71A} cat thrC::GFP-spoIVA^{T70A,T71A} spec* Δ*spoVK::erm pyrD::spoVK cat::tet*	This study
TD854	Δ*spoIVA::neo amyE::spoIVA^{K30E} cat thrC::GFP-spoIVA^{K30E} spec* Δ*spoVK::erm pyrD::spoVK cat::tet*	This study
TD848	Δ*spoIVA::neo amyE::spoIVA^{D97A} cat thrC::GFP-spoIVA^{D97A} spec* Δ*spoVK::erm pyrD::spoVK^{A5V} cat::tet*	This study
TD849	Δ*spoIVA::neo amyE::spoIVA^{T70A,T71A} cat thrC::GFP-spoIVA^{T70A,T71A} spec* Δ*spoVK::erm pyrD::spoVK^{A5V} cat::tet*	This study
TD855	Δ*spoIVA::neo amyE::spoIVA^{K30E} cat thrC::GFP-spoIVA^{K30E} spec* Δ*spoVK::erm pyrD::spoVK^{A5V} cat::tet*	This study
JB103	Δ*spoIVA::neo thrC::spoIVA^{D97A} spec*	This study
TD604	*amyE::spoVK-linker-GFP cat*	This study
TD652	Δ*spoIVA::neo amyE::spoVK-linker-GFP cat*	This study
TD675	Δ*spoVK::erm amyE::spoVK cat pyrD::spoVK-linker-GFP cat::tet*	This study
TD682	Δ*spoIVA::neo thrC::spoIVA^{D97A}* Δ*spoVK::erm amyE::spoVK cat pyrD::spoVK-linker-GFP cat::tet*	This study
TD684	Δ*spoIVA::neo thrC::spoIVA^{T70A,T71A}* Δ*spoVK::erm amyE::spoVK cat pyrD::spoVK-linker-GFP cat::tet*	This study

TD836	Δ*spoIVA::neo thrC::spoIVA*^{K30E} Δ*spoVK::erm amyE::spoVK cat pyrD::spoVK-linker-GFP cat::tet*	This study
TD557	Δ*spoIVA::neo thrC::spoIVA*^{D97A} *spec amyE::spoVK cat*	This study
TD558	Δ*spoIVA::neo thrC::spoIVA*^{D97A} *spec amyE::spoVK*^{A5V} *cat*	This study
TD563	Δ*spoIVA::neo thrC::spoIVA*^{T70A,T71A} *spec amyE::spoVK cat*	This study
TD564	Δ*spoIVA::neo thrC::spoIVA*^{T70A,T71A} *spec amyE:: spoVK*^{A5V} *cat*	This study
TD859	Δ*spoIVA::neo thrC::spoIVA*^{K30E} *spec amyE::spoVK cat*	This study
TD860	Δ*spoIVA::neo thrC::spoIVA*^{K30E} *spec amyE:: spoVK*^{A5V} *cat*	This study
TD574	Δ*spoVK::erm amyE::spoVK*$^{\Delta 2\text{-}42}$ *cat*	This study
TD575	Δ*spoVK::erm amyE::spoVK*^{K105A,T106A} *cat*	This study
TD576	Δ*spoVK::erm amyE::spoVK*^{D162A,E163A} *cat*	This study
TD578	Δ*spoVK::erm amyE::spoVK*^{R218A,R276A} *cat*	This study
TD597	*amyE::spoVK cat*	This study
TD598	*amyE::spoVK*$^{\Delta 2\text{-}42}$ *cat*	This study
TD599	*amyE::spoVK*^{K105A,T106A} *cat*	This study
TD600	*amyE::spoVK*^{D162A,E163A} *cat*	This study
TD602	*amyE::spoVK*^{R218A,R276A} *cat*	This study
TD883	*amyE::P*$_{spoVID}$*-spoVK*^{D162A,E163A}*-His*$_6$ *cat*	This study
TD884	*amyE::P*$_{spoVID}$*-spoVK*^{D162A,E163A}*-FLAG cat*	This study
TD1193	*amyE::P*$_{spoVID}$*-spoVK*^{A5V,D162A,E163A}*-FLAG cat*	This study
TD651	Δ*spoVID::neo amyE::spoVK-linker-GFP cat*	This study
TD695	Δ*spoVID::neo amyE::spoVID*^{T532G} *cat pyrD::spoVK-linker-GFP cat::tet*	This study
TD1257	Δ*spoIVA::erm* Δ*spoVID::neo thrC::spoIVA spec amyE::spoVID*$^{501\text{-}575}$ *pyrD::spoVK-linker-GFP cat::tet*	This study
KR394	Δ*spoIVA::neo thrC::spoIVA spec*	Ramamurthi et al., 2006
JB171	Δ*spoIVA::erm* Δ*spoVID::neo thrC::spoIVA spec*	This study
JB174	Δ*spoIVA::erm* Δ*spoVID::neo thrC::spoIVA spec amyE::spoVID cat*	This study
TD892	Δ*spoIVA::erm* Δ*spoVID::neo thrC::spoIVA spec amyE::spoVID*$^{501\text{-}575}$	This study
TD893	Δ*spoIVA::erm* Δ*spoVID::neo thrC::spoIVA spec amyE::spoVID*$^{526\text{-}575}$	This study
TD1268	Δ*spoIVA::erm* Δ*spoVID::neo thrC::spoIVA spec amyE::P*$_{spoVID}$*-spoVK*$^{D162A\text{-}E163A}$*-FLAG cat*	This study
TD1281	Δ*spoIVA::erm* Δ*spoVID::neo thrC::spoIVA spec amyE:: P*$_{spoVID}$*-spoVK*$^{D162A\text{-}E163A}$*-FLAG cat sacA::GFP-spoVID*$^{501\text{-}575}$ *cat::tet*	This study
TD1267	Δ*spoIVA::neo thrC::spoIVA spec amyE:: P*$_{spoVID}$*-spoVK*$^{D162A\text{-}E163A}$*-FLAG cat*	This study
TD1277	Δ*spoIVA::neo thrC::spoIVA spec amyE:: P*$_{spoVID}$*-spoVK*$^{D162A\text{-}E163A,\Delta 2\text{-}6}$*-FLAG cat*	This study
TD1283	Δ*spoIVA::neo thrC::spoIVA spec amyE:: P*$_{spoVID}$*-spoVK*$^{D162A\text{-}E163A,A5V}$*-FLAG cat*	This study
TD1278	Δ*spoIVA::erm* Δ*spoVID::neo thrC::spoIVA spec amyE::P*$_{spoVID}$*-spoVK*$^{D162A\text{-}E163A,\Delta 2\text{-}6}$*-FLAG cat*	This study
TD1284	Δ*spoIVA::erm* Δ*spoVID::neo thrC::spoIVA spec amyE:: P*$_{spoVID}$*-spoVK*$^{D162A\text{-}E163A,A5V}$*-FLAG cat*	This study
SC765	*amyE::P*$_{spoVM}$*-SpoVM-Iphluorin-cat*	This study
SC766	*amyE::P*$_{spoIIQ}$*-Iphluorin-cat*	This study
SC767	*amyE::P*$_{spoVM}$*-Iphluorin-cat*	This study
SC777	*thrC::P*$_{hyperspank}$*-Iphluorin-erm*	This study

Escherichia coli strains used in this study		
Strain	Genotype and description	Reference
BL21(DE3)	*pTD211* (*pET28a* backbone, P_{T7}-*spoVK-His*$_6$)	This study
BL21(DE3)	*pTD308* (*pET28a* backbone, P_{T7}- *spoVK*^{D162A,E163A}-*His*$_6$)	This study

841

842

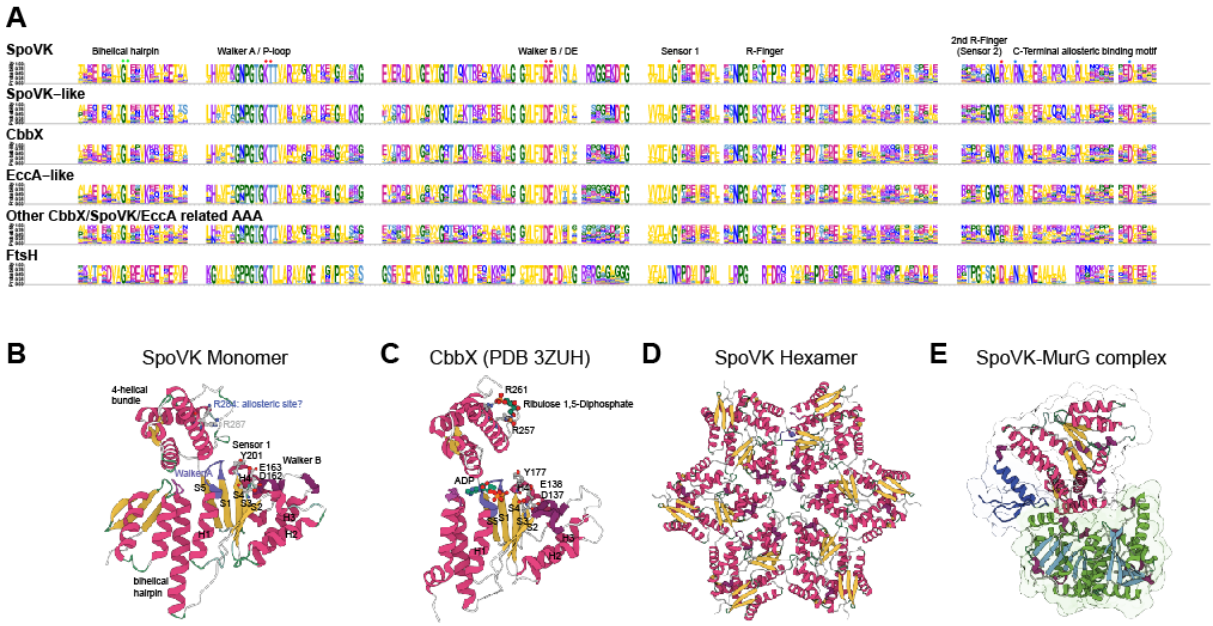

Figure S1. Sequence and structural comparison between SpoVK and members of the SpoVK-EccA-like AAA+ ATPase clade. (A) Sequence logo displaying conservation of amino acid residues in the SpoVK-EccA-like AAA+ ATPase clade. Letters represent amino acid abbreviations; height of each letter represents the probability of conservation among orthologs of the family. The first and second arginine fingers are marked with red dots. Blue dots are conserved residues contacting the allosteric ligand ribulose bisphosphate. (B-E) Cartoon depictions of (B) AlphaFold2 prediction of SpoVK structure, (C) CbbX from *Cereibacter sphaeroides* (PDB 3ZUH), (D) AlphaFold-Multimer prediction of SpoVK hexamer, and (E) AlphaFold-Multimer prediction of SpoVK-MurG complex.

843

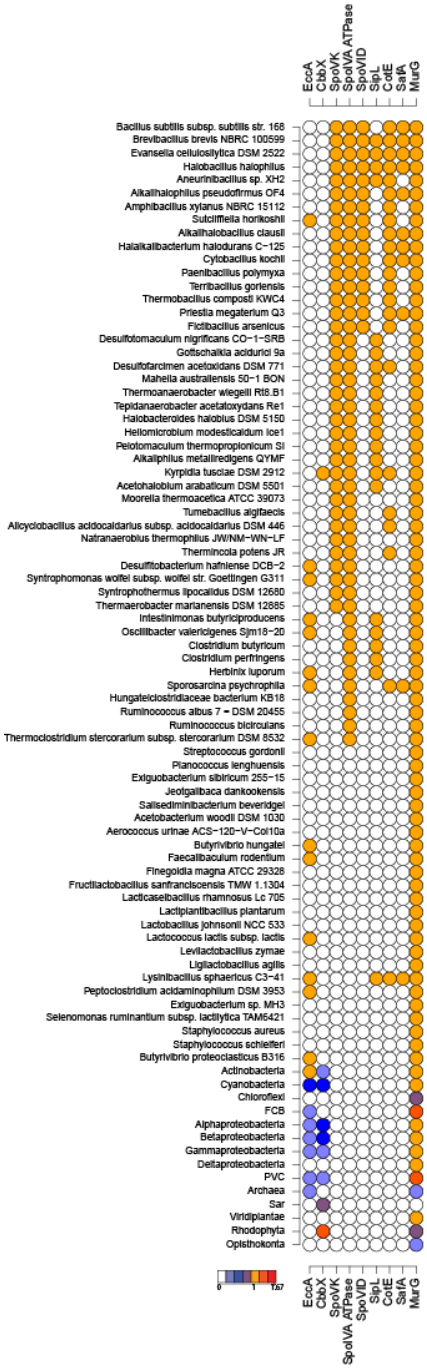

Figure S2. Phyletic pattern vectors of EccA, CbbX, SpoVK, SpoIVA ATPase, SpoVID, SipL, CotE, SafA, and MurG domain proteins. The presence or absence of the protein in the clade or organism (Firmicutes) are shown. The legend shows the color gradient for normalized counts that were scaled by square root.

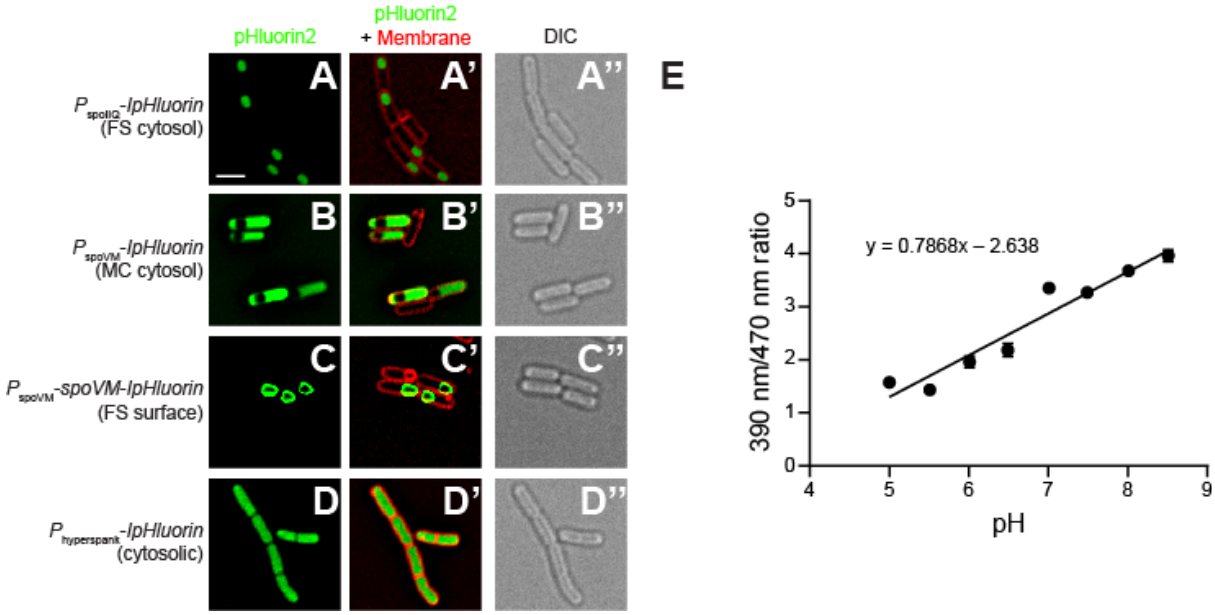

Figure S3. Subcellular localization of various lpHluorin constructs during sporulation. Fluorescence micrographs of *B. subtilis* (A-C'') at t = 4 h after induction of sporulation producing (A-A'') lpHluorin in the forespore, expressed under control of the *spoIIQ* promoter, (B-B'') lpHluorin in the mother cell, expressed under control of the *spoVM* promoter, or (C-C'') SpoVM-lpHluorin at the forespore surface, expressed in the mother cell under control of the *spoVM* promoter; or (D-D'') during vegetative growth producing lpHluorin, expressed under control of an IPTG-inducible promoter at t = 2 h after IPTG induction. (A-D) fluorescence from lpHluorin; (A'-D') overlay, lpHluorin and membranes visualized using FM4-64; (A''-D'') differential interference contrast. Strains: SC765, SC766, SC767, and SC777. Scale bar: 2 µm. (E) Calibration curve of ratio of fluorescence emission at 510 nm when excited at either 390 nm or 470 nm ratio as a function of media pH.

845

846